TITLE:

Linear ubiquitination‐induced necrotic tumor remodeling elicits immune evasion

AUTHOR(S):

Sasaki, Katsuhiro; Hayamizu, Yoshie; Murakami, Ryuji; Toi, Masakazu; Iwai, Kazuhiro

京都大学学術情報リポジトリ
KURENAI
Kyoto University Research Information Repository

京都大学
KYOTO UNIVERSITY

FEBS
Letters

FEBS PRESS
science publishing by scientists

RESEARCH LETTER

Linear ubiquitination-induced necrotic tumor remodeling elicits immune evasion

Katsuhiro Sasaki[1], Yoshie Hayamizu[1], Ryuji Murakami[2,3], Masakazu Toi[4] and Kazuhiro Iwai[1]

1 Department of Molecular and Cellular Physiology, Graduate School of Medicine, Kyoto University, Japan
2 Alliance Laboratory for Advanced Medical Research, Graduate School of Medicine, Kyoto University, Japan
3 Discovery Accelerator, Astellas Pharma Inc, Ibaraki, Japan
4 Breast Cancer Unit, Graduate School of Medicine, Kyoto University Hospital, Japan

Tumor-elicited inflammation confers tumorigenic properties, including cell death resistance, proliferation, or immune evasion. To focus on inflammatory signaling in tumors, we investigated linear ubiquitination, which enhances the nuclear factor-κB signaling pathway and prevents extrinsic programmed cell death under inflammatory environments. Here, we showed that linear ubiquitination was augmented especially in tumor cells around a necrotic core. Linear ubiquitination allowed melanomas to tolerate the hostile tumor microenvironment and to extend a necrosis-containing morphology. Loss of linear ubiquitination resulted in few necrotic lesions and growth regression, further leading to repression of innate anti-PD-1 therapy resistance signatures in melanoma as well as activation of interferon responses and antigen presentation that promote immune-mediated tumor eradication. Collectively, linear ubiquitination promotes tumor-specific tissue remodeling and the ensuing immune evasion.

Keywords: cell death; immune evasion; inflammation; linear ubiquitination; LUBAC; tumor necrosis

Ubiquitination is an important post-translational modification. The existence of different protein-conjugated ubiquitin chains and their recognition by a plethora of signaling adapter proteins regulate cellular behavior, fate, and environmental adaptation [1,2]. The formation of atypical linear ubiquitin chains by head-to-tail polymerization serves as a key mediator of inflammatory nuclear factor (NF)-κB signaling [3,4]. In addition, linear ubiquitination acts as a potent suppresser of programmed cell death in response to multiple types of extracellular stimulants, including tumor necrosis factor (TNF), interleukin (IL)-1β, and Toll-like

Abbreviations
Ab, antibody; ADP, adenosine di-phosphate; AEC, adenylate energy charge; APC, allophycocyanin; CC, cleaved caspase; CDR, complementarity determining region; CK, cytokeratin; CSCC, cutaneous squamous cell carcinoma; CTL, cytotoxic T-lymphocyte; DAMP, damage-associated molecular pattern; DAPI, 4′,6-diamidino-2-phenylindole; DEGs, differentially expressed genes; DOX, doxycycline; ELISA, enzyme-linked immunosorbent assay; EMT, epithelial–mesenchymal transition; FAO, fatty acid β-oxidation; FCCP, carbonylcyanide-*p*-trifluoromethoxyphenylhydrazone; FDR, false discovery rate; FFPE, formalin-fixed, paraffin-embedded; FITC, fluorescein; GEC, guanylate energy charge; GEO, gene expression omnibus; GO, gene ontology; GSEA, gene set enrichment analysis; H&E, hematoxylin–eosin; IDC, invasive ductal carcinoma; IF, immunofluorescence; IHC, immunohistochemistry; IL, interleukin; IPRES, innate anti-PD-1 therapy resistance; Iso, isotype control; ISR, integrated stress response; ISREs, interferon-stimulated response elements; KD, knockdown; LUBAC, linear ubiquitin chain assembly E3 ligase complex; mt, mitochondrial; NES, normalized enrichment score; NF, nuclear factor; NK, natural killer; numDEInCat, number of DEGs in each GO category; O/E, overexpression; OCR, oxygen consumption rate; OVA, ovalbumin; OXPHOS, oxidative phosphorylation; PCA, principal component analysis; PerCP-Cy, peridinin chlorophyll protein-cyanine; ROS, reactive oxygen species; sg, single guide; TCA, tricarboxylic acid; TLR, Toll-like receptor; TME, tumor microenvironment; TNF, tumor necrosis factor; TRE, tetracycline responsive element; TUNEL, TdT-mediated dUTP nick end labeling; Ub, ubiquitin; VH, heavy-chain variable domain; VL, light-chain variable domain.

receptor (TLR) ligands, which are frequently detected in solid tumors [4–6]. Studies in humans and rodents have demonstrated that linear ubiquitin chains are essential for the cytokine-mediated regulation of organismal homeostasis and protection from cell-death-induced systemic inflammation [7–11]. However, although malignant cancers assume a persistent inflammatory environment promoting linear ubiquitination, the exact mechanisms underlying the role of linear ubiquitination in tumorigenesis remain largely unknown and were investigated in this study [12,13].

Materials and methods

Animal experiments and tumor challenge

All animal care and experiments were performed in accordance with protocols approved by the Animal Research Committee, Graduate School of Medicine, Kyoto University, and complied with all ethical regulations. The mice were housed at the Institute of Laboratory Animals, Kyoto University, under specific pathogen-free conditions, and all animal experiments were conducted in accordance with the Kyoto University guidelines for animal experiments.

Pulmonary tumors were established by intravenously injecting 1×10^6 murine osteosarcoma cell line (LM8) cells, resuspended in Hanks Balanced Salt Solution (Sigma, St. Louis, MO, USA), into C3H mice (SLC, Shizuoka, Japan). In the subcutaneous transplantation experiments, either 2 or 5×10^5 tumor cells were resuspended in Hanks Balanced Salt Solution (Sigma), mixed with Matrigel (Corning, Corning, NY, USA) at a ratio 1 : 1, and then injected into the following types of age-matched (7–12-week-old) syngeneic allogeneic or xenogeneic model mice: Balb/c (SLC), C57BL/6 (SLC), NSG (#005557; Jackson Lab, Bar Harbor, ME, USA), $Rag2^{-/-}$ (CIEA, Kanagawa, Japan), $Tcra^{-/-}$ (#002116; Jackson Lab), $Ifng^{-/-}$ (#002287; Jackson Lab), or $Ifng^{-/-}Tnf^{-/-}$ (crossed $Ifng^{-/-}$ with #003008; Jackson Lab). After subcutaneous transplantation, caliper-based tumor measurements were taken two or three times per week, and the tumor volume was estimated using the standard formula: $V = \pi/6 \times$ (length) $L \times$ width (W) $\times$ height (H). Tetracycline responsive element (TRE)-mediated *Rbck1* knockdown (KD) within a subcutaneous tumor was induced by the supplementing the animals' drinking water with 200 mg·L^{-1} doxycycline (DOX). The anti-PD1 antibody treatment experiments involved administering 200 µg anti-PD-1 antibody (29F.1A12; BioXcell, Lebanon, NH, USA) three times per day, every other day, starting at the time point of tumor mass appearance (Day 12 or 24, respectively) to mice bearing B16-F10 or sg*Rnf31* tumors. For natural killer (NK) cell depletion, an anti-NK1.1 antibody (PK136; BioXcell) was intraperitoneally injected into mice on Days 1, 0, and 3 (100 µg) and twice a week (200 µg) during tumor development.

Human tissue samples

To assess linear ubiquitination across a broad range of cancers, we purchased a human cancer tissue array (BCN963b; US Biomax, Rockville, MD, USA), on which multiple organ tumors and adjacent normal tissues were placed, as depicted in Fig. S2a. For linear ubiquitin staining, focusing on the cancer cells surrounding the necrotic core, we collected formalin-fixed, paraffin-embedded (FFPE) blocks of necrotic clinical human cancer tissue from BioIVT, Westbury, NY, USA; skin squamous cell carcinoma (ID: 77253A2, STMR : SNML : SNCR : SOTR = 30 : 30 : 40 : 0) and breast infiltrating ductal carcinoma (ID: 120548A2, STMR : SNML : SNCR : SOTR = 50 : 0 : 40 : 10). For each specimen, the terms STMR, SNML, SNCR, and SOTR refer to the estimated percentages of tumor, non-neoplastic/normal, necrotic, and "something other," tissues, respectively. Preparation of the cancer tissue slides from these blocks was performed by the Center for Anatomical Pathological and Forensic Medical Research in Kyoto University. The breast cancer tissue samples used in the peptide competition assay were collected from patients with written informed consent. This study was approved by the Ethics Committee for Clinical Research, Kyoto University Hospital (approval number: G424), and the Astellas Research Ethics Committee (approval number: 000090).

Cell lines and generation of CRISPR/Cas9-edited, overexpression- or knockdown-inducible tumor cells

B16-F10 (murine melanoma) and 4T1 (murine mammary adenocarcinoma) cell lines were obtained from JCRB Cell Bank, Osaka, Japan. HCT116 (human colorectal carcinoma), SW620 (human colon adenocarcinoma), and A375 (human melanoma) cell lines were obtained from ATCC. The LM8 (murine osteosarcoma with high lung metastatic potential) cell line was kindly provided by H. Yoshikawa (Osaka University) [14]. The MOC2 (murine oral squamous cell carcinoma) cell line was kindly provided by R. Uppaluri (Dana-Farber Cancer Institute) [15,16]. These cell lines were maintained in the recommended culture media containing 10% FBS at 37 °C, 5% CO_2. Gene targeting of B16-F10 was performed using the CRISPR/Cas9 system. The CRISPR guide RNAs for each gene were designed by BENCHLING, San Francisco, CA, USA. The following procedures were performed as previously described [17]. For the simultaneous double knockout of two different cytokine receptors, the px458-BFP plasmid was constructed by replacing the *GFP* gene (cloned into the px458 plasmid; Addgene, Watertown, MA, USA) with the *TagBFP* gene. The px458-BFP plasmid was used for the expression of one cytokine receptor, while the original px458 plasmid was used for the other. Genetic knockdown of intracellular proteins or cell-surface cytokine receptors was confirmed by

western blot or flow cytometry, respectively. The following flow cytometry antibodies were used: allophycocyanin (APC)-anti-TNFR1 (55R-286; BioLegend, San Diego, CA, USA), Biotin-anti-IFNAR1 (MAR1-5A3; BioLegend), Biotin-anti-IFNGR1 (2E2; BioLegend), and Streptavidin APC conjugate (17-4317-82; Thermo Fisher Scientific, Waltham, MA, USA). The CRISPR sgRNA sequences were as follows (5′–3′): *Rnf31*, GTGGTCCGCTGCAACGCTCAT; *Sharpin*, GTGGCAGTGCACGCGGCGGTC; *Rbck1*, GAGTACGCCCGGATATGACAG; *Tnfrsf1a*, TGTCACGGTGCCGTTGAAGC; *Ifngr1*, ATTAGAACATTCGTCGGTAC; *Ifnar1*, GCTCGCTGTCGTGGGCGCGG; *Chuk*, ACTGACGTTCCCGAAACCGC; *Ikbkb*, GGGAAATGAAAGAACGCCTG; *Ikbkg*, TGGGTGAAGAATCTTCTCTG; *Nfkb1*, TGTGAAGGCCCATCACACGG; *Rela*, GATTCCGCTATAAATGCGAG. For gene transduction, the cDNA encoding chicken ovalbumin (OVA) or the UBAN domain of the murine NF-?B essential modulator (NEMO) was subcloned into the lentivirus-based vector, CSII-EF-IRES2-Bsd (RIKEN). For tdTomato labeling, the Venus-encoding gene in CSII-EF-IRES2-Venus (RIKEN) was replaced with the tdTomato-encoding gene. And 2 μg of each CSII plasmid, along with 1 μg of pxPAX2 (Addgene) and 1 μg of pMD2.G (Addgene), was transfected into packaging 293T cells. After 3 days, the B16-F10 cells were infected with the culture supernatant and selected by addition of 2 μg·mL^{-1} blasticidin to the culture medium. Exogenous gene expression was detected by western blotting or flow cytometry. For DOX-inducible knockdown, the lentivirus-based shRNA vector pTRIPZ-Venus, in which the puromycin-encoding resistance gene in the original pTRIPZ (Horizon Discovery, Cambridge, UK) plasmid was replaced with the Venus-encoding gene, was used according to manufacturer's instructions. The following synthesized oligos were phosphorylated, annealed, and inserted (using the XhoI and EcoRI restriction sites) into the pTRIPZ-Venus vector for miR30-based shRNA construction [18]: murine *Rbck1*; Sense: 5′-TCGAGAAGGTATATTGCTGTTGACAGTGAGCGAGCAGACGACAGAGATGCTAAA TAGTGAAGCCACAGATGTATTTAGCATCTCTGTCGTCTGCCTGCCTACTGCCTCGG-3′, Antisense: 5′-AATTCCGAGGCAGTAGGCAGGCAGACGACAGAGATGCTAAATACATCTGTGGCTTCACTATTTAGCATCTCTGTCGTCTGCTCGCTCACTGTCAACAGCAATATACCTTC-3′, non-silencing; Sense: 5′-TCGAGAAGGTATATTGCTGTTGACAGTGAGCGATCTCGCTTGGGCGAGAGTAAGTAGTGAAGCCACAGATGTACTTACTCTCGCCCAAGCGAGAGTGCCTACTGCCTCGG-3′, Antisense: 5′-AATTCCGAGGCAGTAGGCACTCTCGCTTGGGCGAGAGTAAGTACATCTGTGGCTTCACTACTTACTCTCGCCCAAGCGAGATCGCTCACTGTCAACAGCAATATACCTTC-3′. Selective knockdown of the *Rbck1* gene was observed by quantitative PCR (Fig. S3e).

Creation of linear-ubiquitin-specific antibody

The linear-ubiquitin-specific antibody, 1E3.v2, was produced as previously described [19,20]. Briefly, the heavy-chain variable domain (VH) of linear ubiquitin Fab (PDB ID: 3U30C) was fused to human IgG1 CH1 domain and rabbit IgG CH2 + CH3 domain (for monovalent antibody) or human IgG1 CH1 plus hinge domain and rabbit IgG CH2 + CH3 domain (for divalent antibody). The light-chain variable domain (VL) of linear ubiquitin Fab (PDB ID: 3U30C) was fused to the human kappa CL domain. Each synthesized IgG1 heavy-chain or kappa light-chain DNA construct was inserted into the pcDNA3.4 vector (Thermo Fisher Scientific). The vectors were then co-transfected into ExpiCHO cells (Thermo Fisher Scientific) for transient expression. The IgGs were purified from the supernatant using protein A beaded agarose resin (MabSelect SuRe; Cytiva, Marlborough, MA, USA).

Immunohistochemistry and immunofluorescence

Tumors or normal organ tissues were immediately fixed with a buffer solution containing 10% formalin. The lung was prefixed by perfusion of the fixation solution via the trachea, using a SURFLO ETFE intravenous Catheter (Terumo, Tokyo, Japan). The tissues were then embedded in paraffin wax to prepare FFPE blocks. The thin sections were deparaffinized and incubated in AR9 buffer (Akoya, Marlborough, USA) at 99 °C for 15 min using a microwave tissue processor (Azumayaika, Tokyo, Japan) for antigen retrieval. To inactivate the endogenous horse radish peroxidase (HRP), sections were immersed in methanol containing 30% H_2O_2 for 10 min at room temperature (RT). For immunohistochemistry (IHC) staining, the section was blocked with serum included in the ImmPRESS Polymer Detection Kit (Vector Lab, Newark, CA, USA) and processed according to the manufacturer's instructions. Specifically, the sections were stained with ImmPACT Vector Red (Vector Lab) or the DAKO Liquid DAB$^+$ Substrate Chromogen System (Agilent Technologies, Santa Clara, CA, USA). Hematoxylin was used for counterstaining. Photomicrographs were acquired on an Olympus BX51 upright microscope, using UPlan Apo 10×/0.40, UPlan Apo 20×/0.70, and UPlan Fl 40×/0.75 objective lenses (Olympus, Tokyo, Japan). For immunofluorescence (IF) staining, the sections were blocked with blocking buffer (2% bovine serum albumin [BSA], 0.1% TritonX-100 in PBS) containing 5% goat serum. The blocked sections were stained overnight at 4 °C with antibodies diluted in blocking buffer, and they were incubated for 1 h at RT with an AlexaFluor-conjugated antibody (Thermo Fisher Scientific) diluted in blocking buffer. After an additional incubation with 1 μg·mL^{-1} DAPI for 5 min, the labeled sections were preserved in ProLong Diamond Antifade Mountant

(Thermo Fisher Scientific). Photomicrographs were acquired on a Keyence Fluorescence Microscope BZ-9000, using CFI Plan Apo 40× 0.95/0.14 mm and Plan Apo λ 60× 1.40 Oil objective lenses (Nikon, Tokyo, Japan). The observed signals were processed using the BZ-II image analysis application (Keyence, Osaka, Japan), and the acquired images were analyzed with FIJI software. Linear ubiquitin foci were automatically counted using the following settings: size 5–100 pixels, circularity 0.3–1.0. To calculate the extent of cleaved caspase-3 and TUNEL staining, and thus the size of the hypoxic area (as a percentage of the total tumor area), sections were stained without counterstaining. After splitting the image data channels and setting the FIJI threshold, the area of positive staining per field was automatically quantified. The images were acquired from three distinct tissue samples, and the data were pooled from at least five images of a single section. The following antibodies were used for IHC and IF: anti-K48-linked polyubiquitin (Apu2; Merck, Darmstadt, Germany), anti-K63-linked polyubiquitin (Apu3; Merck), anti-Linear-linked polyubiquitin (1E3.v2, home-prepared; 1E3; Merck), anti-CD31 (SZ31; Dianova, Hamburg, Germany), anti-Pan-Cytokeratin (AE-1/AE-3; BioLegend), anti-Ki67 (SP6; Abcam, Cambridge, UK), anti-Cleaved Caspase-3 Asp175 (#9661; Cell Signaling, Danvers, MA, USA), anti-Fibronectin (ab2413; Abcam), anti-mouse IFNγ (bs-0480R; Bioss, Woburn, MA, USA), anti-Phospho-STAT1 Tyr701 (58D6; Cell Signaling), anti-CD11b (EPR1344; Abcam), anti-F4/80 (Cl:A3-1; Bio X Cell), and IRF4 (#62834; Cell Signaling).

Peptide competition assay

A peptide competition assay was used to assess the specificity of the anti-linear ubiquitin chain antibody (1E3.v2). The antibody was neutralized by incubating with a penta-linear ubiquitin peptide (Enzo Life Sciences, Farmingdale, NY, USA) for 1 h. Then, breast tumor serial sections were then stained with the native or neutralized 1E3.v2 antibody. The detailed IF staining procedure is outlined in "Immunohistochemistry and immunofluorescence" methods section. Photomicrographs were acquired on a Carl Zeiss confocal Fluorescence Microscope LSM710, using Objective Plan Apo 63× 1.4 Oil DIC M27 (Carl Zeiss, Oberkochen, Germany). Maximum intensity projections were obtained using ZEN2010 software (Carl Zeiss).

TUNEL staining

Deparaffinized tissue sections were treated for 1 h at RT with proteinase K, followed by HRP inactivation using 30% H_2O_2/methanol for 10 min at RT. TUNEL staining was performed using the TUNEL Assay Kit (Abcam), according to manufacturer's instructions.

Hypoxia cell staining

The Hypoxyprobe-1 Plus Kit (HPI) was used to measure hypoxia in tumors, according to manufacturer's instructions. In brief, pimonidazole was resuspended in PBS and intraperitoneally injected into mice at 60 µg·g^{-1} mouse weight 1 h before dissection. The FFPE sections were deparaffinized and treated with a fluorescein (FITC)-conjugating anti-pimonidazole antibody. To enable observation under an optical microscope, the sections were further incubated with an HRP-conjugated anti-FITC antibody, followed by staining with the DAKO Liquid DAB$^+$ Substrate Chromogen System (Agilent Technologies).

Flow cytometry analysis of tumor-associated macrophages

The 4×10^5 B16-F10 cells were subcutaneously transplanted into mice. After 2 weeks, the tumors were collected, minced, and dissociated in RPMI containing DNase I (0.5 mg·mL^{-1}; Worthington, Lakewood, NJ, USA) and collagenase D (1 mg·mL^{-1}; Roche, Basel, Switzerland). After gentle rotation for 10 min in a 37 °C incubator, the tumor suspension was thoroughly sieved through cell strainers (40 µm pore size) to collect all tumor-infiltrating cells. After erythrolysis, some of the tumor suspension was subjected to Fc-blocking using anti-CD16/32 antibody (93; BioLegend) for 5 min at 4 °C and then staining with antibodies against macrophage surface markers for 15 min at 4 °C. Next, the cells were stained using Zombie Aqua Fixable Viability Kit (BioLegend) for dead cell detection and then acquired on a FACS Canto II flow cytometer (BD Biosciences, Franklin Lakes, NJ, USA). Flow cytometry data were analyzed using FLOWJO software (v10.8.1; BD Biosciences). The following fluorochrome-conjugated antibodies were used: phycoerythrin (PE)-anti-CD24 (M1/69; BioLegend), peridinin chlorophyll protein-cyanine (PerCP-Cy)5.5-anti-Ly6C (HK1.4; BioLegend), APC-anti-F4/80 (BM8; BioLegend), PE-Cy7-anti-CD11b (M1/70; BioLegend), biotin-anti-CD206 (C068C2; BioLegend), APC-Cy7-anti-Streptavidin (BD Biosciences), and BV421-anti-CD45 (30-F11; BD Biosciences).

RNA sequencing and data processing

For RNA sequencing (RNA-seq), total RNA from fresh tumors was purified by a sequential isolation step, in which the extraction of pre-clean RNA step was performed using ISOGEN (Nacalai Tesque, Kyoto, Japan) and the column-based purification step was performed using the RNeasy Mini Kit (Qiagen, Hilden, Germany). After conducting a quality check (RNA integrity number [RIN] = 9.5–10.0) of the RNA samples on a BioAnalyzer 2100 (Agilent

Technologies), 500 ng of each RNA sample was subjected to strand-specific library preparation with polyA enrichment using the NEBNext Ultra II Directional RNA Library Prep Kit for Illumina (New England Biolabs, Ipswich, MA, USA). Sequencing was performed on the Illumina NovaSeq 6000 platform (Illumina, San Diego, CA, USA) in a 2×150 bp paired-end configuration.

To obtain high-quality, clean data, the adapter and PCR primer sequences, low-quality reads, and read sequence contaminations were filtered out using CUTADAPT (v1.9.1). The clean data were mapped to the ENSEMBL *Mus musculus* GRCm38.100 reference genome using HISAT2 (v2.0.2). HTSEQ (v0.6.1) was then used to count the reads within the target locus and calculate the gene expression levels as fragments per kb per million reads (FPKM) values. Determination of differentially expressed genes (DEGs) between control samples and sg*Rnf31* B16-F10 tumors was performed using the DESEQ2 BIOCONDUCTOR package (v1.6.3); the adjusted *P*-value (P_{adj}) of genes was set at < 0.05 (Fig. 3H; Fig. S5c). Gene ontology (GO) terms, including three ontologies describing the molecular function, cellular component, and biological process of the gene, which were enriched among the DEGs, were identified using GOSEQ (v1.34.1), with a *P*-value < 0.05. The significantly up- and down-regulated biological terms (according to the GO enrichment analysis) were presented, along with the false discovery rate (FDR) and the number of DEGs in each GO category (numDEInCat) (Fig. S8d). To find distinct gene sets significantly enriched among the DEGs, the gene set enrichment analysis (GSEA) method (Broad Institute) was used to estimate the absolute enrichment score for each of the previously validated MSigDB gene signatures: the hallmark (H) gene sets and the cell type signature (C8) gene sets. The meaningful GSEA biological terms were presented along with the corresponding FDR, normalized enrichment score (NES), and gene set size (Figs S6a and S7a). The RNA-seq data were visualized as bubble and volcano plots using PRISM (v9.4.0; GraphPad, Boston, MA, USA).

Spheroid formation

The 5×10^5 tumor cells were resuspended in 300 µL Matrigel (Corning), plated in a 24-well plate, and incubated for 30 min at 37 °C to form a gel. After addition of 500 µL Dulbecco's Modified Eagle Medium (DMEM) + 10% FBS to each well, the cells were cultured for 4 days.

Cytokine measurement

B16-F10 or MOC2 tumors were generated in $Ifng^{-/-}Tnf^{-/-}$ mice for 3 weeks after cell inoculation. And 100 mg of each frozen tumor tissue was homogenized in 0.5 mL RIPA buffer (50 mM Tris pH 8.0, 150 mM NaCl, 1% NP-40, 1%

SDC, and 0.1% SDS) at 3000 r.p.m. for 15 s using a Multi-beads shocker (Yasui Kikai, Osaka, Japan). After centrifugation at 20,000 g for 10 min at 4 °C, the purified lysates were quantified using the Bradford Assay BCA Kit (Nacalai Tesque) and the protein concentration was adjusted to 10 mg·mL^{-1}. The lysates were subjected to an enzyme-linked immunosorbent assay (ELISA MAX; BioLegend) for the detection of interferon (IFN)-γ or tumor necrosis factor (TNF) concentration, according to manufacturer's instructions.

Quantitative PCR

RNA isolation from cultured cells was performed using the column-based RNeasy Mini Kit (Qiagen), according to manufacturer's protocols. In the case of tumor samples, pre-cleaned RNA from fresh or frozen tumor tissues was extracted using ISOGEN (Nacalai Tesque) and further purified using the RNeasy Mini Kit. Reverse transcription and subsequent quantitative PCR were performed as described previously [17]; the following primers were used: *Tnf*; Sense: 5′-TTCTGTCTACTGAACTTCGGGGTGAT CGGTCC-3′ and Antisense: 5′-GTATGAGATAGCAAAT CGGCTGACGGTGTGGG-3′, *Nfkbia*; Sense: 5′-GCCA GGAATTGCTGAGGCACTT-3′ and Antisense: 5′-GTCT GCGTCAAGACTGCTACAC-3′, *Actb*; Sense: 5′-CATTG CTGACAGGATGCAGAAGG-3′ and Antisense: 5′-TGC TGGAAGGTGGACAGTGAGG-3′, *Rnf31*; Sense: 5′-GCCCTGAGGTGGGATTCTG-3′ and Antisense: 5′-TT GAGGTAGTTTCGAGGCTCC-3′, *Rbck1*; Sense: 5′-CT GCTATCAAGTATGCCACCTG-3′ and Antisense: 5′-TG TGCATGTACGCATCCTCC-3′, *Ifnb1*; Sense: 5′-GCCTTT GCCATCCAAGAGATGC-3′ and Antisense: 5′-ACCTGT CTGCTGGTGGAGTTC-3′ *Ifng*; Sense: 5′-TGAACGCT ACACACTGCATCTTGG-3′ and Antisense: 5′-CGACT CCTTTTCCGCTTCCTGAG-3′, *Ppargc1a*; Sense: 5′-TGA TGTGAATGACTTGGATACAGACA-3′ and Antisense: 5′-GCTCATTGTTGTACTGGTTGGATATG-3′ for total PGC-1α, Sense: 5′-GGACATGTGCAGCCAAGACTC-3′ and Antisense: 5′-CACTTCAATCCACCCAGAAAGCT-3′ for the PGC-1α1 isoform, Sense: 5′-CCACCAGAATGA GTGACATGGA-3′ and Antisense: 5′-GTTCAGCAAGA TCTGGGCAAA-3′ for the PGC-1α2 isoform, Sense: 5′-AAGTGAGTAACCGGAGGCATT-3′ and Antisense: 5′-TTCAGGAAGATCTGGGCAAAGA-3′ for the PGC-1α3 isoform. *Irf1*; Sense: 5′-ATGCCAATCACTCGAATGCG-3′ and Antisense: 5′-TTGTATCGGCCTGTGTGAATG-3′, *Irf4*; Sense: 5′-TCCGACAGTGGTTGATCGAC-3′ and Antisense: 5′-CCTCACGATTGTAGTCCTGCTT-3′, *Irf8*; Sense: 5′-CGGGGCTGATCTGGGAAAAT-3′ and Antisense: 5′-CACAGCGTAACCTCGTCTTC-3′, *b2m*; Sense: 5′-CCCCACTGAGACTGATACATACG-3′ and Antisense: 5′-CGATCCCAGTAGACGGTCTTG-3′, *H2-K1*; Sense: 5′-GTGATCTCTGGCTGTGAAGT-3′ and Antisense: 5′-GT

CTCCACAAGCTCCATGTC-3′, *H2-D1*; Sense: 5′-AGTGG TGCTGCAGAGCATTACAA-3′ and Antisense: 5′-GGTG ACTTCACCTTTAGATCTGGG-3′, *Tapbp*; Sense: 5′-GG CCTGTCTAAGAAACCTGCC-3′ and Antisense: 5′-CCACC TTGAAGTATAGCTTTGGG-3′, *Cxcl10*; Sense: 5′-GCCGT CATTTTCTGCCTCAT-3′ and Antisense: 5′-GCTTCCCT ATGGCCCTCATT-3′.

Fluorescent *in situ* hybridization

Detection of intratumoral mRNAs was performed using the RNA-Scope Multiplex Fluorescent V2 Assay Kit (Advanced Cell Diagnostics, Newark, CA, USA), according to manufacturer's instructions for FFPE tissue samples. In brief, tumors were sliced into 5 µm thick sections from a fresh FFPE tissue block. After deparaffinized by xylene and 100% ethanol, the sections were treated with hydrogen peroxide for 10 min at RT and then with antigen retrieval solution for 15 min at 99 °C. For antigen retrieval, additional protease treatment was performed for 30 min at 40 °C. After washing, each of the target probes, Mm-*Ifng* (#311391; Advanced Cell Diagnostics) and Mm-*Tnf*-O1-C2 (#844961-C2; Advanced Cell Diagnostics), was hybridized for 2 h at 40 °C for signal amplification and then detected by fluorescent Opal deposition (Opal 520 for *Ifng* and Opal 690 for *Tnf*). The samples were then stained with a tdTomato antibody (PM005; MBL, Tokyo, Japan) for 1 h at RT and then with a Alexa Fluor-546-conjugated anti-rabbit IgG (Thermo Fisher Scientific) to enable the detection of tdTomato+ tumor cells within tissues. Photomicrographs were acquired on a BZ-9000 fluorescence microscope (Keyence) with objective lenses Plan Apo λ 60× 1.40 Oil and Plan Apo l 100× 1.45 Oil (Nikon). The observed signals were processed using the BZ-II image analysis application (Keyence), and the acquired images were analyzed using FIJI software. The fluorescent foci counts were automatically calculated using the following setting: size 5–100 pixels, circularity 0.3–1.0.

In vivo survival competition assay

Venus or tdTomato intracellular fluorescent proteins were introduced into wild-type or CRISPR/Cas9-edited B16-F10 cells by lentiviral transduction. The labeled cells were then examined and purified using a FACS Aria III cell sorting system (BD Biosciences). After at least two passages *in vitro*, control (Venus+) and tdTomato+ tumor cells were harvested and mixed at a 1 : 1 ratio. The mixed cells were immediately implanted, along with Matrigel extracellular matrix (Corning), into mice (1×10^5 cells per mouse). After 2 weeks, the tumors were collected, minced, and dissociated in RPMI containing DNase I (0.5 mg·mL^{-1}; Worthington) and collagenase D (1 mg·mL^{-1}; Roche) using a gentle MACS tissue dissociator (Miltenyi Biotec, Bergisch

Gladbach, Germany), followed by agitation for 30 min at 37 °C. After erythrolysis, tumor cells were sieved through cell strainers (100 µm pore size) to remove undigested tissues and debris. Some of the cell suspension was acquired on a FACS Canto II flow cytometry (BD Biosciences) to determine the Venus:tdTomato tumor cell ratios *in vivo*.

In vitro cytokine stimulation

Tumor cells suspended in DMEM + 10% FBS were plated into 24-well plates (2×10^4/well). The cells were then treated with combinations of the following cytokines: (a) TNF (10 ng·mL^{-1}, 410-MT-050; R&D, Minneapolis, MN, USA), IFN-α (20 ng·mL^{-1}, 130-093-131; Miltenyi Biotec), IFN-β (20 ng·mL^{-1}, CYT-651; Prospec, Rehovot, Israel), and IFN-γ (20 ng·mL^{-1}, 130-105-782; Miltenyi Biotec) for mouse cells; and (b) TNF (10 ng·mL^{-1}, HZ-1014; Protein-Tech, Rosemont, IL, USA), IFN-β (20 ng·mL^{-1}, HZ-1298; ProteinTech), and IFN-γ (20 ng·mL^{-1}, HZ-1301; Protein-Tech) with or without 10 µM of the HOIPin-8 LUBAC inhibitor (Astellas Pharma Inc.) for human cells [21]. The treated cells were then collected and stained with 1 µM SYTOX Green (Thermo Fisher Scientific) for 30 min at 4 °C and acquired on the FACS Canto II flow cytometer (BD Biosciences).

In vitro T-cell killing assay

A full-length copy of OVA was introduced into each CRISPR/Cas9-edited B16-F10 cell by lentiviral transduction, and its expression was determined by western blotting. The transduced cells were plated into 24-well plates (2×10^4/well) in DMEM + 10% FBS and co-cultured with pre-activated OT-1 CD8+ T cells at the indicated effector to target (E : T) ratios for 48 h at 37 °C, 5% CO$_2$. The total cells were stained with 1 µM SYTOX Green (Thermo Fisher Scientific) and an APC-Cy7-conjugated anti-mouse CD45 antibody (BioLegend) for 30 min at 4 °C, followed by flow cytometry analysis. During data analysis, the CD45+ T cells were gated out to precisely quantify dead tumor cells.

Ex vivo restimulation of OT-T cells

A cell suspension of splenocytes isolated from OT-I transgenic mice was prepared (5×10^6 mL^{-1}) in RPMI + 10% FBS, supplemented with 2 mM L-glutamine (Thermo Fisher Scientific), 50 µM 2-mercaptoethanol, and 25 mM HEPES, pH7.5. Following the addition of 2 µg·mL^{-1} OVA peptide SIINFEKL, the cells were seeded into 24-well plates (1 mL/well) and incubated at 37 °C, 5% CO$_2$. During stimulation with OVA peptide, the cells were monitored daily and maintained by addition of fresh medium or passaging.

After a 3-day expansion period, the OT-I T cells were purified using mouse CD8a microbeads (Miltenyi Biotec), according to manufacturer's instructions. The sorted CD8$^+$ cells were then co-cultured with tumor target cells in the T-cell killing assay.

Transmission electron microscopy

Transmission electron microscopy (TEM) imaging was supported by the Division of Electron Microscopic Study, Center for Anatomical Studies, Graduate School of Medicine, Kyoto University. Tumors or cultured cells were embedded in Matrigel and fixed with a solution containing 2% glutaraldehyde (Nacalai Tesque) and 4% paraformaldehyde in 0.1 M PBS, pH 7.4 (Wako, Osaka, Japan) at 4 °C. After washing with 0.1 M PBS, the samples were post-fixed with 1% of osmium tetraoxide in 0.1 M PBS for 2 h, dehydrated with a serially diluted ethanol solution, and embedded in epoxy-resin Luveak-812 (Nacalai Tesque). Once polymerized, the samples were cut into ultrathin sections (60–80 nm thick) on an ultramicrotome EM UC7 (Leica, Wetzlar, Germany) and stained with 1% uranyl acetate and alkaline lead citrate. The ultrathin sections were examined with a JEM-1400 Flash transmission electron microscope (JEOL, Tokyo, Japan).

Mitochondrial isolation from B16-F10 tumors

Transplanted tumors were dissected 2 weeks after inoculation into mice. The tumors were minced in three volumes of 0.2% fatty-acid-free BSA-containing MSHE buffer (70 mM sucrose, 210 mM mannitol, 5 mM HEPES, and 1 mM EGTA, pH 7.2) and then gently homogenized (50 strokes) using a precooled glass Dounce Homogenizer. Homogenates were centrifuged at 1000 g for 3 min at 4 °C. The supernatants were separated by additional centrifugation at 12 000 g for 10 min at 4 °C. After the pellets were washed with BSA + MSHE buffer and resuspended in MSHE buffer without BSA, the isolated mitochondria were quantified using the Bradford Assay BCA Kit (Nacalai Tesque).

Measurement of oxygen consumption rate

The oxygen consumption rates (OCRs) of tumor-tissue-derived mitochondria were measured by using the Seahorse XFe96 Analyzer (Agilent Technologies), according to manufacturing instructions. After plating 4 μg of mitochondria/well into a 96-well microplate, and centrifugation at 2000 g for 20 min at 4 °C, MAS buffer (70 mM sucrose, 220 mM mannitol, 10 mM KH$_2$PO$_4$, 5 mM MgCl$_2$, 2 mM HEPES, 1 mM EGTA, and 0.2% fatty-acid-free BSA) containing rotenone (final 2 μM) and succinate (final 10 mM) was added. Changes in the mitochondrial OCRs (in pmol·min^{-1})

were measured at 37 °C in quadruplicate per sample, before and after the sequential addition of 4 mM adenosine diphosphate (ADP), 2 μM oligomycin, 2 μM carbonylcyanide-*p*-trifluoromethoxyphenylhydrazone (FCCP), and 4 μM antimycin A. ADP depletion was not observed during measurements, meaning that ADP-driven mitochondrial respiration was highly maintained until the injection of oligomycin.

Evaluation of mitochondrial DNA copy number

Total DNA was extracted from each tumor using DNeasy Blood & Tissue Kits (Qiagen). Mitochondrial (mt)DNA copy number was estimated by PCR-based relative quantification of mtDNA-encoding NADH dehydrogenase 1 (*ND1*) and nuclear hexokinase 2 (*HK2*) as normalization controls. The following primers were used: Sense 5′-CTAGCAGAAACAAACCGGGC-3′ and Antisense 5′-CCGGCTGCGTATTCTACGTT-3′ for *ND1*, and Sense 5′-GCCAGCCTCTCCTGATTTTAGTGT-3′ and Antisense 5′-GGGAACACAAAAGACCTCTTCTGG-3′ for *HK2*.

Flow cytometry analysis of mitochondrial content

B16-F10 cells in DMEM + 10% FBS were plated into 48-well plates (1 × 10^5/well). The next day, the cells were labeled with 0.1 μM MitoTracker Deep Red (Thermo Fisher Scientific) for 30 min at 37 °C, and then acquired on a FACS Canto II flow cytometer (BD Biosciences).

Western blotting

The B16-F10 cells were lysed on ice with lysis buffer (0.1 M Tris pH 8.0, 0.15 M NaCl, 1% NP-40, and 0.5% TritonX-100) containing 1 mM EDTA and the protease inhibitor cocktail (Roche) and then centrifuged at 20 000 g for 5 min at 4 °C. Fresh tumors were washed with cold PBS, minced in a 5× volume of lysis buffer containing 1 mM EDTA, 50 mM *N*-ethylmaleimide (Nacalai Tesque), and the protease inhibitor cocktail (Roche), and then homogenized (10 strokes) using a precooled glass Dounce Homogenizer. The homogenates were centrifuged at 7500 g for 5 min at 4 °C, and the supernatants were further purified by centrifugation at 20 000 g for 5 min at 4 °C. The purified lysates were subjected to SDS/PAGE and immunoblotting, as described previously [17]. Chemiluminescent signals were detected using an Amersham Imager 680 analyzer (Cytiva). Antibodies against components of the linear ubiquitin chain assembly complex (LUBAC) were described previously [17]. The other antibodies were commercially purchased: anti-ubiquitin (P4D1; Santa Cruz, Dallas, TX, USA), anti-β-actin (AC-74; Sigma), anti-K48-linked polyubiquitin (Apu2; Merck), anti-K63-linked polyubiquitin (Apu3; Merck), and anti-Fibronectin (ab2413; Abcam).

Metabolite extraction from tumor tissues

Approximately 200 mg of frozen tissue was placed in a homogenization tube, along with zirconia beads (5 and 3 mmφ). Next, 6500 μL of 50% acetonitrile/Milli-Q water containing internal standards (H3304-1002; Human Metabolome Technologies, Yamagata, Japan) was added to the tube. The tissue was then completely homogenized at 1100 r.p.m., 4 °C for 7 × 120 s using a bead shaker (Shake Master NEO; Bio Medical Science, Tokyo, Japan). The homogenate was then centrifuged at 2300 ***g***, 4 °C for 5 min. Subsequently, 400 μL of the upper aqueous layer was centrifugally filtered through a Millipore 5-kDa cutoff filter (UltrafreeMC-PLHCC; Human Metabolome Technologies) at 9100 ***g***, 4 °C for 120 min, to remove macromolecules. The filtrate was completely dried under vacuum and reconstituted in 50 μL of Milli-Q water for metabolome analysis by Human Metabolome Technologies.

Metabolome analysis

Metabolome analysis was conducted using capillary electrophoresis time-of-flight mass spectrometry (CE-TOFMS) for cation analysis and CE-tandem mass spectrometry (CE-MS/MS) for anion analysis, based on the methods described previously [22,23]. Briefly, CE-TOFMS and CE-MS/MS analysis were carried out using an Agilent CE capillary electrophoresis system equipped with an Agilent 6210 TOF mass spectrometer (Agilent Technologies) and Agilent 6460 Triple Quadrupole LC/MS (Agilent Technologies), respectively. The systems were controlled by Agilent G2201AA CHEMSTATION software version B.03.01 for CE (Agilent Technologies) and connected by a fused silica capillary (50 μm *i.d.* × 80 cm total length) with commercial electrophoresis buffer (H3301-1001 and I3302-1023 for cation and anion analyses, respectively; Human Metabolome Technologies) as the electrolyte. The TOF mass spectrometer was set to scan from 50 to 1000 mass-to-charge ratio (m/z) [22], and the triple quadrupole mass spectrometer was used to detect compounds in dynamic multiple reaction monitoring (MRM) mode. Peaks were extracted using the MASTERHANDS automatic integration software (Keio University) [24] and MASSHUNTER QUANTITATIVE ANALYSIS B.04.00 (Agilent Technologies) in order to obtain peak information including m/z, peak area, and migration time (MT). Signal peaks were annotated according to the metabolite database, based on their m/z values and MTs. The peak area of each metabolite was normalized to internal standards, and the metabolite concentration was evaluated by standard curves with three-point calibrations using each standard compound. Principal component analysis (PCA) was performed using the R program.

Determination of bioenergy index

The adenylate energy charge (AEC) and guanylate energy charge (GEC), both indicators of cellular energy production, were defined as reported previously [25,26]; the formulae were as follows: $AEC = [ATP] + 0.5 \times [ADP]/[ATP] + [ADP] + [AMP]$ and $GEC = [GTP] + 0.5 \times [GDP]/[GTP] + [GDP] + [GMP]$.

Statistical analysis

Values were represented as the mean ± standard deviation of the mean (SEM). Statistical significance was assessed by two-tailed unpaired Student's *t*-tests (for comparisons of two groups) and ordinary one-way analysis of variance (ANOVA) followed by the Dunnett's test or two-way ANOVA followed by the Tukey's test (for multiple comparisons). PRISM 9 software (GraphPad) was used for all statistical analyses. A *P*-value < 0.05 was considered as a measure of statistical significance.

Datasets and figure generation

Heatmaps were generated using HEATMAPPER (http://www.heatmapper.ca/expression/). Graphs, including volcano plots and bubble plots, were generated using PRISM 9 (GraphPad). Figures were created in MICROSOFT POWERPOINT software (v16.66.1, Microsoft, Redmond, WA, USA), ADOBE ACROBAT PRO (v2020.005.30407, Adobe, San Jose, CA, USA), and CANVAS X DRAW (7.0.3, Canvas GFX, Boston, MA, USA). Additional codes can be obtained from the corresponding author upon reasonable request.

Code availability

RNA-Seq data processes or metabolome analysis using standard software programs were conducted by Azenta Life Sciences or by Human Metabolome Technologies, respectively, thus there are restrictions on the detailed script availability.

Results

Tumors accelerate linear ubiquitination

Our initial aim was to examine whether the amount of linear ubiquitin chains was higher in solid tumors than in healthy tissues. Since the linear chain is barely detectable upon the absence of proinflammatory stimuli, we prepared a linear-ubiquitin-chain-specific antibody with a similar high affinity to the one reported in recent excellent studies and conducted immunohistological staining [19,20] (Fig. S1a–d). Using this antibody on transplanted murine B16-F10 melanoma cells, we detected linear ubiquitin chains as tiny globular foci (< 1 μm diameter) (Fig. S1e). These foci have been previously observed in cytokine-treated cultured cells [27], and were unlike the diffuse staining patterns of
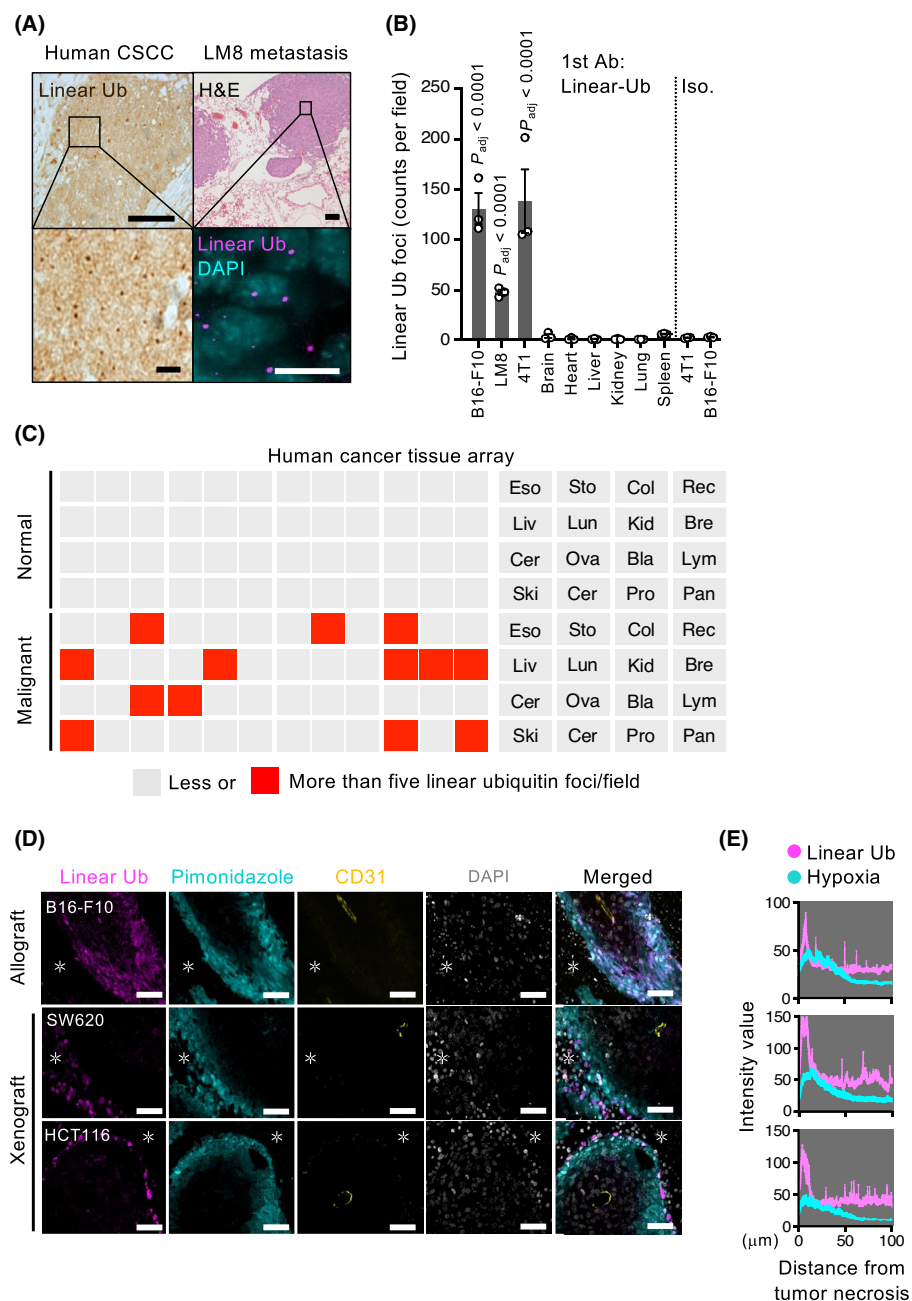
Fig. 1. Tumor cells exhibit high levels of linear ubiquitination, especially at the necrotic periphery. (A) Histological detection of linear ubiquitin. Immunohistochemistry of human CSCC, and immunofluorescent staining of pulmonary metastases of a murine LM8 osteosarcoma cell line. For LM8, a hematoxylin and eosin staining image is also shown in the upper right panel. Scale bars, 100 μm (upper), 10 μm (lower). (B) Counts of linear ubiquitin foci in tumor specimens from several syngeneic mouse tumor models or unaffected control BALB/c tissues. Data were averaged over three biologically independent samples and at least five distinct fields per sample. Data are presented as the mean ± SEM. One-way ANOVA, followed by Dunnett's multiple comparisons test, was used for statistical analysis. (C) Summary of linear ubiquitin staining of a human cancer tissue array containing various cancer types and the corresponding normal tissues, as indicated. The red or gray solid box indicates a higher (> 5 linear ubiquitin foci per field) or lower (< 5 linear ubiquitin foci per field) level of linear ubiquitination in the tissues, respectively. The representative images are shown in (Fig. S2a). (D) Co-immunofluorescent staining of linear ubiquitin and hypoxic cells (using an anti-pimonidazole antibody) in B16-F10 (an allograft model), SW620, or HCT116 (xenograft models) tumor specimens. CD31; blood vessel marker. Asterisks indicate tumor necrosis area. Scale bars, 50 μm. Data were averaged over two independent samples. (E) Intensity of linear ubiquitin (magenta) or pimonidazole (cyan) staining of tumor cells at the necrotic tissue/viable tissue boundary, calculated from the data shown in (D).

K48 or K63 ubiquitin chains. We also detected linear ubiquitin foci in other established murine tumor transplantation models and in samples from patients with cutaneous squamous cell carcinoma (CSCC) (Fig. 1A, B). Moreover, the cancer tissue array revealed that a wide range of human solid tumors, but not the corresponding non-inflamed normal tissues, preferentially produced linear ubiquitin chains (Fig. 1C; Fig. S2a). These results imply that enhanced linear ubiquitination in response to tumor-elicited inflammation is a common feature of most solid tumors.

Detailed microscopic observation of developing allograft or xenograft tumors revealed that linear ubiquitin chains preferentially localized in cells at the boundary between the viable and the dying tumor tissues (Fig. 1D). Dying tumor tissues formed a necrotic core, which likely arose as a result of oxygen and nutrient deprivation. The addition of pimonidazole, an exogenous hypoxia marker, confirmed that the linear-

ubiquitin-positive cells were mainly localized at the leading edge of the hypoxic tumor tissue (Fig. 1D,E). Furthermore, the increased expression of linear ubiquitin chains at the hypoxic/viable tissue boundaries was also observed in clinical samples from patients with CSCC or breast invasive ductal carcinoma (IDC) (Fig. S2b,c). Considering that mass cell death releases proinflammatory factors, these results imply that linear ubiquitination is specifically triggered by the necrotic environment established within aggressive solid tumors.

LUBAC loss sensitizes tumors to immune attack

To examine the role of linear ubiquitination in tumorigenesis, we established a *Rnf31*-depleted (single guide [sg]*Rnf31*) B16-F10 murine melanoma cell line. *Rnf31* encodes HOIP, a catalytic subunit of the linear ubiquitin chain assembly E3 ligase complex (LUBAC). Thus,
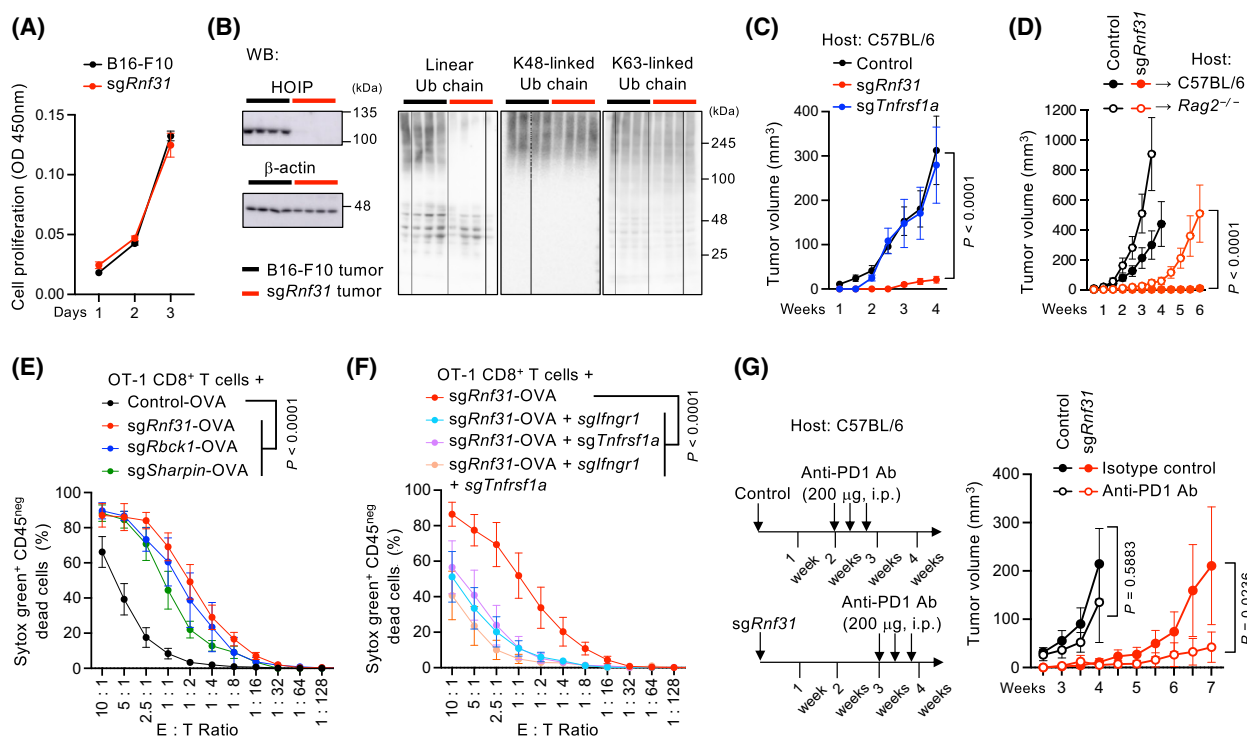

Fig. 2. Linear ubiquitin loss sensitizes tumors to immune-mediated attack. (A) Proliferation of *in vitro* cultured control and sg*Rnf31* B16-F10 cells. (B) Western blot analysis of linkage-specific ubiquitin chains (linear, K48, and K63) and HOIP in the indicated tumor lysates ($n = 4$ independent samples per group). β-actin was used as a loading control. (C, D) Tumor size measurements in C57BL/6 (C: Control $n = 9$, sg*Rnf31* $n = 6$, sg*Tnfrsf1a* $n = 8$; D: Control $n = 8$, sg*Rnf31* $n = 7$) or *Rag2*$^{-/-}$ (D: Control $n = 8$, sg*Rnf31* $n = 8$) recipient mice. (E, F) T-cell cytotoxicity assay using LUBAC-compromised B16-F10 with (E) or without (F) expression of the indicated cytokine receptors. The percentages of dead cells within the CD45$^-$ population after a 48 h co-culture with OT-1 effector CD8$^+$ T cells are depicted. (G) Tumor size measurements after administration of anti-PD-1 antibody ($n = 6$–8 independent tumors per group). Data are presented as the means ± SEM. For A, B, E, F, data were averaged over three independent experiments. Two-way ANOVA, followed by Tukey's multiple comparisons test, was used for statistical analysis of data in C–G.

HOIP expression was lost from the sg*Rnf31* cells, leading to LUBAC dysfunction (Fig. S3a) [17]. We demonstrated that sg*Rnf31* cells could proliferate *in vitro* as effectively as wild-type B16-F10 cells (Fig. 2A). However, the loss of linear ubiquitination capacity markedly suppressed tumor growth when the sg*Rnf31* cells were transplanted into syngeneic C57BL/6 mice (Fig. 2B,C). Moreover, the competitive blockade of linear ubiquitin-mediated signaling by the overexpression of linear ubiquitin-binding UBAN (ubiquitin binding in ABIN and NEMO) domain suppressed tumor development (Fig. S3b–d). Besides, we found that doxycycline (DOX)-inducible LUBAC depletion by targeting the other two LUBAC subunits (HOIL-1L and SHARPIN) in growing tumors destabilized LUBAC and impaired tumor growth (Fig. S3e,f). These results strongly indicate that linear-ubiquitin-mediated signaling is only activated when the tumor assumes a three-dimensional conformation and is essential for tumor development.

We next assessed the effect of intratumoral linear ubiquitin loss on tumor immune vulnerability. When the sg*Rnf31* B16-F10 cells were injected into *Rag2*$^{-/-}$ mice lacking mature T and B lymphocytes, tumor growth was partially restored (Fig. 2D). Moreover, the antibody-induced depletion of natural killer (NK) cells also considerably enhanced tumor progression (Fig. S4a). In an *ex vivo* setting, we found that defective LUBAC activity highly sensitized chicken ovalbumin (OVA)-expressing B16-F10 cells to killing by OT-1 CD8^{+} T cells recognizing the OVA peptide-H2-K^{b} complex (Fig. 2E). The well-defined inhibitory function of linear ubiquitination in the extrinsic apoptotic pathway prompted us to focus on the role of cytokines and their cognate receptors in cytotoxic T-lymphocyte (CTL)-mediated killing. Deletion of either *Tnfrsf1a* or *Ifngr1* (encoding the TNF and interferon [IFN]-? receptors, respectively) completely inhibited the CTL-mediated killing of sg*Rnf31* B16-F10 cells (Fig. 2F). This protective effect was even greater in cells where both receptors were deleted, indicating that TNF and IFN-? acted synergistically (Fig. 2F). Consistent with this observation, the combined treatment with TNF, IFN-γ, and/or type I IFN (i.e., IFN-α and -β), which were highly expressed within tumors, killed cultured sg*Rnf31* B16-F10 or *Braf*^{V600E} human melanoma cell lines treated with a LUBAC inhibitor much more effectively than treatment with each cytokine alone (Fig. S4b–d). We next treated sg*Rnf31*-tumor-transplated C57BL/6 mice with an anti-PD-1 antibody, which functions as an immune checkpoint inhibitor. As expected, the anti-PD-1 antibody potently inhibited the proliferation of sg*Rnf31* cells (Fig. 2G). Taken

together, these results reveal that linear ubiquitination in tumors predominantly suppresses cell death triggered by immune-cell-derived cytokines, and that its loss increases the vulnerability of tumors to immune attack.

Cell death tolerance shapes the necrotic TME

In highly immunodeficient NOD-*scid Il2γ*$^{-/-}$ (NSG) mice, which have no mature lymphocytes or NK cells, the growth rate of control and sg*Rnf31* B16-F10 tumors was substantially improved (Fig. 3A). However, a growth difference was still observed between the control and sg*Rnf31* B16-F10 tumors, which was confirmed by differences in the expression of proliferation marker Ki67 (Fig. 3A,B). Although immune vulnerability underscored sg*Rnf31* tumor regression, its contribution to the suppression of tumorigenesis appeared only partial. These results further encouraged us to consider the possibility that linear ubiquitination elicited other pro-tumorigenic effects. To our surprise, histological analyses revealed that the tumor necrotic area (comprised of dead and dying tumor cells) shrank considerably when the sg*Rnf31* tumors were placed in a poorly immunogenic environment (Fig. 3C). Moreover, immunohistochemical staining of active caspase-3 or fragmented DNA confirmed that the number of apoptotic cells within the sg*Rnf31* tumors was much lower than in the size-matched control tumors (Fig. 3D,E).

We next observed an increase in linear ubiquitination levels in tumor cells at the viable tissue/necrotic tissue interface, which is constitutively exposed to cytotoxic immune attack (Fig. 1D,E; Fig. S2b,c). Since linear-ubiquitin-mediated protection against cell death is induced by inflammatory stimuli [4–6], we hypothesized that enhanced linear ubiquitination enables cancer cells to better adapt to the necrotic tumor microenvironment (TME). Thus, the intratumoral survival of two cell lines (control Venus^{+} and tdTomato^{+} CRISPR/Cas9-edited B16-F10 cells) was assessed in an identical necrotic TME using an *in vivo* cell competition assay (Fig. S5a). As was observed in the tumor cell line engraftment experiments, a reduction in LUBAC levels (by depletion of SHARPIN and/or HOIL-1L) or its complete loss significantly attenuated the survival of tumor cells in the TME (Fig. S5b,c). Additionally, we demonstrated that the reduced survival of the LUBAC-deficient tumor cells was not caused by the down-regulation of NF-κB signaling; the deletion of NF-κB transcription factors, p50 and p65 (RelA), or one of the IκB kinase (IKK) subunits had no overt effect on tumor cell survival (Fig. S5d).
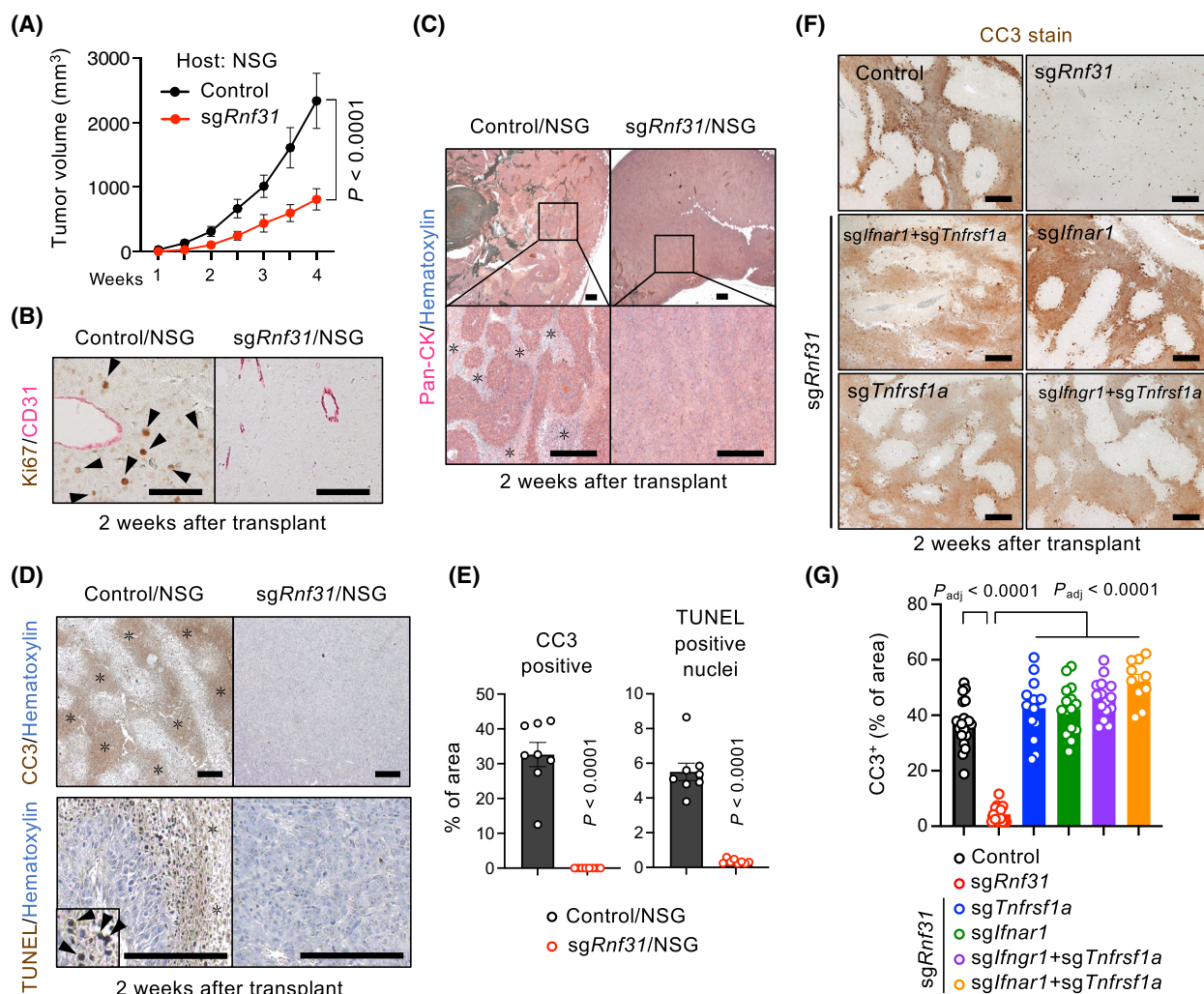
Fig. 3. Linear ubiquitin prompts necrotic tumor remodeling. (A) Tumor size measurements in immunodeficient NSG mice as recipients. Control $n = 8$, sg*Rnf31* $n = 9$. Two-way ANOVA, followed by Tukey's multiple comparisons test, was used for statistical analysis. (B) Immunohistochemistry staining for proliferation marker Ki-67 in the indicated tumors. CD31; blood vessel marker. Scale bars, 100 μm. Data are representative of three independent samples. (C) Immunohistochemistry staining for pan-cytokeratin (Pan-CK; epithelial-tumor-specific marker) with hematoxylin counter stain. The magnified images are shown in the lower panels. Scale bars, 400 μm. Data are representative of two independent samples. (D) Histological detection of cleaved caspase-3 (CC3)- or TUNEL-positive dying tumor cells in the indicated tissue sections. (E) Quantification of CC3- or TUNEL-positive tumor cells. The data were pooled from different eight fields of two different tumors. Two-tailed unpaired Student's *t*-test was used for statistical analysis. Scale bars, 200 μm. (F) Immunohistochemistry staining for CC3. Data are representative of at least two independent samples. Scale bars, 200 μm. (G) Quantification of the CC3-positive area in the tumors indicated in (F). The data were pooled from 10 to 20 distinct fields (2–4 independent tumors per group). One-way ANOVA, followed by Dunnett's multiple comparisons test, was used for statistical analysis. Data are presented as the means ± SEM. Asterisks: tumor necrosis area.

However, the deletion of the cytokine receptors, *Tnfrsf1a* or *Ifnar1*, in sg*Rnf31* cells slightly increased tumor survival, while the loss of *Ifngr1* restored tumor survival almost completely (Fig. S5e). These results indicate that IFN-γ is produced in the necrotic TME, and that linear ubiquitin protects tumor cells from IFN-γ-mediated cell death via a mechanism independent of NF-κB signaling.

Since effector T and NK cells are the primary sources of IFN-γ, we next engrafted the tumor cell mixture into two immunodeficient mouse strains, *Tcra*$^{-/-}$ and NSG, which lack almost all IFN-γ-producing cells. We found that the sg*Rnf31* cells were selectively eliminated from these mice following tumor implantation (Fig. S5f). The sg*Rnf31* cells also failed to proliferate in *Ifng*$^{-/-}$ mice, which indicated that

IFN-γ was being secreted by tumor cells (Fig. S5f). Indeed, a substantial amount of IFN-γ could be detected in B16-F10 tumors, but not in the control MOC2 non-immunogenic tumors, engrafted into $Ifng^{-/-}Tnf^{-/-}$ mice (Fig. S5g) [15,16]. Moreover, immunohistochemistry demonstrated that IFN-γ expression was elevated in hypoxic tumor cells at the necrotic border, where linear ubiquitin chains were highly concentrated (Fig. S5h,i). Consistent with these findings, IFN-γ-induced phosphorylated STAT1 (pSTAT1) preferentially accumulated within the tumor necrotic core (Fig. S5j). Furthermore, highly sensitive fluorescence *in situ* hybridization detected IFN-γ transcripts in dying B16-F10 cells (Fig. S5k,l). Consistent with the increased rates of linear ubiquitination at the tumor viable tissue/necrotic tissue border, these data reveal that the IFN-γ responsible for the elimination of sg*Rnf31* cells originated from dying tumor cells within the necrotic core.

As expected, the simultaneous deletion of IFN-γ, TNF, and IFN-β receptors in sg*Rnf31* cells protected the resulting tumor cells from the combined cytotoxic effects of these cytokines (Fig. S5m). When these cytokine-receptor-deficient sg*Rnf31* cells were transplanted in mice, they regained the ability to proliferate and form the necrotic core, as observed in the control tumors (Fig. 3F,G; Fig. S5n). Collectively, these results indicate that linear ubiquitination protects the tumor from synergistic proinflammatory cytokine-mediated cytotoxicity and enables tumor progression via the establishment of a necrotic core and the associated TME.

Gene set enrichment analysis revealed that the genes associated with monocyte and myeloid cell signatures were highly up-regulated in sg*Rnf31* B16-F10 tumors (Fig. S6a). Besides, the transcriptome data demonstrated that macrophage differentiation into the anti-inflammatory M2 subset and the increase of their efferocytotic activity (i.e., the effective clearance of apoptotic cells) occurred in tumors with linear ubiquitin deficiency (Fig. S6b). Indeed, infiltrates of CD206⁺ (M2) macrophages were identified within the necrotic core of sg*Rnf31* tumors (Fig. S6c–e) [28]. Less apoptotic cells were detected in sg*Rnf31* tumors transplanted in the NSG mice than control tumors (Fig. 3C–E). Increased recruitment of the CD206⁺ M2 macrophages in sg*Rnf31*-tumors suggested that the dying sg*Rnf31* cells, which produce proinflammatory cytokines including IFN-γ killing themselves, are actively engulfed and removed by the macrophages. Elimination of the dying sg*Rnf31* cells could prevent from expansion of necrotic core by ablation of cytotoxic cytokines secreted from the dying cells. We, therefore,

concluded that linear ubiquitin deficiency induces both efficient tumor cell death and clearance within the developing tumor, preventing the necrotic TME (Fig. 3C–E).

Necrotic core loss raises the tumor IFN response

We next performed transcriptome analysis to evaluate the phenotypic differences between control and sg*Rnf31* tumors and found that their gene profiles were clearly distinct; 859 up- and 1310 down-regulated genes were identified in the sg*Rnf31* tumors (greater than twofold change, P_{adj} value < 0.05) (Fig. 4A,B). GSEA indicated that linear ubiquitin deficiency activated the IFN-α, IFN-γ, and JAK-STAT3 signaling pathway in sg*Rnf31* tumors (Fig. S7a). GSEA also revealed the increased expression of immune-related genes such as IFN-inducible genes and genes encoding molecules involved in antigen presentation, such as MHC class I genes (i.e., *H2-K1*, *H2-K2*, *H2-D1*, *H2-Q4*, *H2-Q6*, and *H2-Q7*), *Tapbp*, and *β2m*. In addition, the expression of genes encoding the two highly related members of interferon regulatory factors (IRFs), IRF4 and IRF8, was markedly altered in sg*Rnf31* tumors; the sg*Rnf31* B16-F10 tumors lost IRF4 expression, while the levels of IFN-inducible IRF8 were markedly increased (Fig. 4B–D) [29]. IRF4 is highly expressed in lymphoma, myeloma, and malignant melanoma cells, whereby it suppresses the expression of some IFN-inducible genes by binding to the interferon-stimulated response elements (ISREs) within their promoters [30,31]. By contrast, intrinsic tumoral expression of anti-tumorigenic IRF8 is often suppressed during the growth of murine and human metastatic melanoma cells [32]. These results suggest that linear ubiquitin deficiency in melanoma tumors boosts the IFN response and attenuates tumor malignancy.

Furthermore, we found that the expression of IRFs 4 and 8 was tightly correlated with malignant tissue remodeling. This was illustrated by the fact that blockade of extrinsic cytotoxic signaling induced necrotic core formation within sg*Rnf31* tumors and reset the expression levels of the two IRFs (Figs 3F,G and 4E). We showed that IRF4 was expressed in tumor cells regardless of their proximity to the necrotic core although the underlying mechanism remains unknown (Fig. 4D). Moreover, as for IRF4, the expression of the immune-related genes was suppressed following the deletion of the IFN-γ, TNF, and IFN-β receptors, which induced necrotic core formation in sg*Rnf31* tumors (Fig. 3G). Collectively, these data indicate that the development of linear-ubiquitin-dependent tumor necrosis and the subsequent malignant tissue
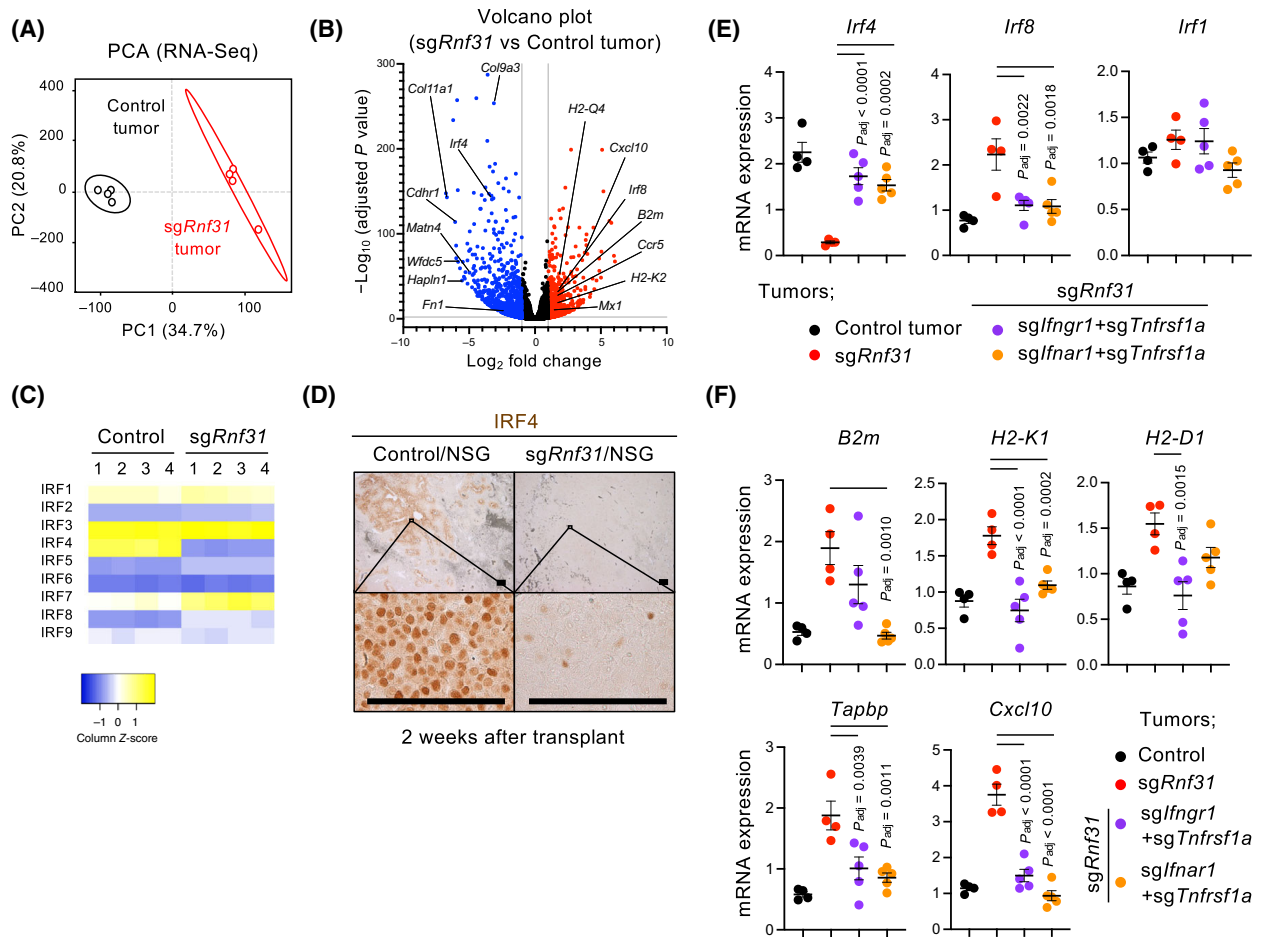
Fig. 4. Linear ubiquitin loss enhances intrinsic IFN responses. (A) Principal component analysis (PCA) of RNA-sequencing data from control and sg*Rnf31* B16-F10 tumors established in NSG mice. $n = 4$ per group. (B) Volcano plot of differentially expressed genes (DEGs) from the transcriptome data of A ($n = 4$ per group). An adjusted P-value (P_{adj}) < 5% and fold-change with a cutoff of 2 were considered significant and indicated as red (up-regulated in sg*Rnf31* tumors) or blue (down-regulated in sg*Rnf31* tumors) dots. (C) Heatmap showing differences in interferon regulatory factor (IRF) expression between control and sg*Rnf31* cells. (D) Immunohistochemistry staining for IRF4 in the indicated tumors. Data are representative of two independent tumors. Scale bars, 200 μm. (E, F) Relative expression levels of IRFs (E) or transcripts involved in the IFN response or antigen presentation (F); control, $n = 4$; sg*Rnf31*, $n = 4$; sg*Ifngr1* + sg*Tnfrsf1a*, $n = 5$; sg*Ifnar1* + sg*Tnfrsf1a*, $n = 5$. Data are presented as the mean ± SEM. One-way ANOVA, followed by Dunnett's multiple comparisons test, was used for statistical analysis.

remodeling alters gene transcription to repress intrinsic IFN responses within the tumor.

Tissue remodeling affects immune resistance

It has been suggested that tumor tissue remodeling affects the TME, oncogenic signaling, and transcriptional regulation [33,34]. Indeed, our GSEA results revealed that several cancer-associated characteristics, including aerobic glycolysis, epithelial–mesenchymal transition (EMT), hypoxia, and the integrated stress response (ISR), were attenuated by the loss of linear

ubiquitination in B16-F10 melanoma cells (Fig. S7a). For example, in stiffened sg*Rnf31* melanoma tumors, the majority of tumor cells had an adequate oxygen supply, as shown by poor pimonidazole accumulation and the decreased expression of hypoxia-responsive genes (Fig. S8a–c). Intriguingly, most of the characteristics observed in sg*Rnf31* tumors were identical to the innate anti-PD-1 therapy resistance (IPRES) signatures, previously reported in melanoma and the other types of cancer [35].

We next performed GO enrichment analysis of the differentially expressed genes (DEGs) between control

and sg*Rnf31* tumors. This revealed that the expression of the genes associated with the extracellular matrix (ECM; i.e., collagen-encoding genes and *Matn3*, *Matn4*, *Wfdc5*, *Wfdc12*, *Hapln1*, and *Fn1*) and cell adhesion molecules (i.e., genes encoding cadherins or protocadherins) was significantly reduced upon loss of linear ubiquitination (Fig. 4B; Fig. S8e,f); of note, these genes are also highly expressed in cells with IPRES signatures. The elevated expression of ECM-related genes is often observed in various solid tumors, where it contributes to the maintenance of tumor stiffness [36]. Moreover, extensive deposits of fibronectin, a key component of the ECM, have been observed within the necrotic core, contributing to TME development (Fig. S8f,g). In general, a dense ECM protects the tumor by acting as a limiting factor for the diffusion of immune cells and cytotoxic molecules (such as therapeutic agents), thereby contributing to tumor progression and resistance to cancer therapy [36]. Thus, the breakdown of ECM observed in sg*Rnf31* tumors could potentially increase the therapeutic efficiency of macromolecular cancer drugs such as the anti-PD-1 antibody [36]. Taken together, these data reveal the pro-tumorigenic potential of linear ubiquitination in melanoma tumors, which helps tumors maintain several IPRES signatures, including tumor stiffness (via increased ECM expression) and escape immune eradication.

Recent comprehensive analyses of immunotherapy-resistant melanoma tumors have revealed a positive correlation between mitochondrial metabolism and the vulnerability of tumors to immune attack [37–39]. We found that the loss of linear ubiquitination also altered the transcription of metabolic enzymes in B16-F10 tumors. Specifically, we observed that linear-ubiquitin-deficient tumor cells had lower levels of glycolysis and higher levels of mitochondrial energy metabolism, including tricarboxylic acid (TCA) cycle, oxidative phosphorylation (OXPHOS), and fatty acid β-oxidation (FAO) than controls (Fig. 5A). Furthermore, metabolomic analysis confirmed the suppression of both aerobic glycolysis and the pentose phosphate pathway (a shunt pathway-producing NADPH and ribose-5-phosphate as precursors of nucleotide biosynthesis) in sg*Rnf31* tumors; however, cellular bioenergy generation was entirely unaffected (Fig. 5B–D; Fig. S9a). In addition, the expression of mitochondrial, but not nuclear, genes was twofold higher in sg*Rnf31* tumors than that in control tumors (Fig. S9b). This implies that mitochondrial oxidative metabolism continued to supply energy to the tumor after linear ubiquitin depletion. In accordance, the sg*Rnf31* tumors exhibited signs of increased mitochondrial biogenesis,

such as higher mitochondrial (mt)DNA copy number, the presence of more mitochondrial tubular structures, elevated expression of the outer mitochondrial membrane protein Tom20, and increased respiration activity (Fig. 5E–G; Fig. S9c–f). Furthermore, the dominance of oxidative metabolism was confirmed in sg*Rnf31* tumors by the increased expression of the antioxidant enzymes, *Sod2* and *Gpx1*, which protected the tumors from high levels of mitochondria-generated reactive oxygen species (ROS) (Fig. 5H). Of note, the increase in mitochondrial numbers and biogenesis was not observed in *in vitro* cultured sg*Rnf31* cells, indicating that the three-dimensional TME was required for mitochondrial involvement in tumorigenesis (Fig. 5E, F; Fig. S9d,g,h). Besides, two isoforms of the transcriptional coactivator PGC-1α (i.e., PGC-1α2 and PGC-1α3), both of which are critical for mitochondrial biogenesis in melanoma cells, were predominantly expressed in the sg*Rnf31* tumors and not in the controls, suggesting that linear ubiquitin deficiency induced dominant oxidative metabolism in B16-F10 tumors (Fig. S9i,j) [40,41].

In addition to the reduced expression of factors associated with antigen presentation (e.g., β2m and MHC class I) (Fig. 4G), we found that the blockade of cytokine signaling, which induced a necrotic TME, suppressed the transcription of metabolic molecules such as OXPHOS or the upregulation of genes implicated in FAO (i.e., *Cox5a* or *Acat1*) in sg*Rnf31* tumors (Fig. 5I). Decreased mitochondrial biogenesis was observed in sg*Rnf31* tumors lacking IFN-γ, TNF, and IFN-β cytokine receptors, which was confirmed by the more spherical mitochondrial morphology (i.e., higher mitochondrial circularity ratio, calculated from the mitochondrial cross-sectional area) and the decreased expression of Tom20 and PGC-1α (Fig. 5I; Fig. S9d,f). Taken together, these results indicate that linear ubiquitination maintains the necrotic TME by protecting tumor cells from cytokine-mediated killing. The tumor tissue remodeling in turn prompts the enrichment of IPRES signatures based on metabolic plasticity and TME-induced gene regulation in tumor cells, which enables the tumor to potentially evade the immune response.

Discussion

In this study, we revealed that linear polyubiquitination protects tumors from cytokine-mediated cytotoxicity. We showed that the absence of linear ubiquitin chains in murine and human melanoma cells markedly promoted tumor cell death in response to the synergistic effects of proinflammatory cytokines, including
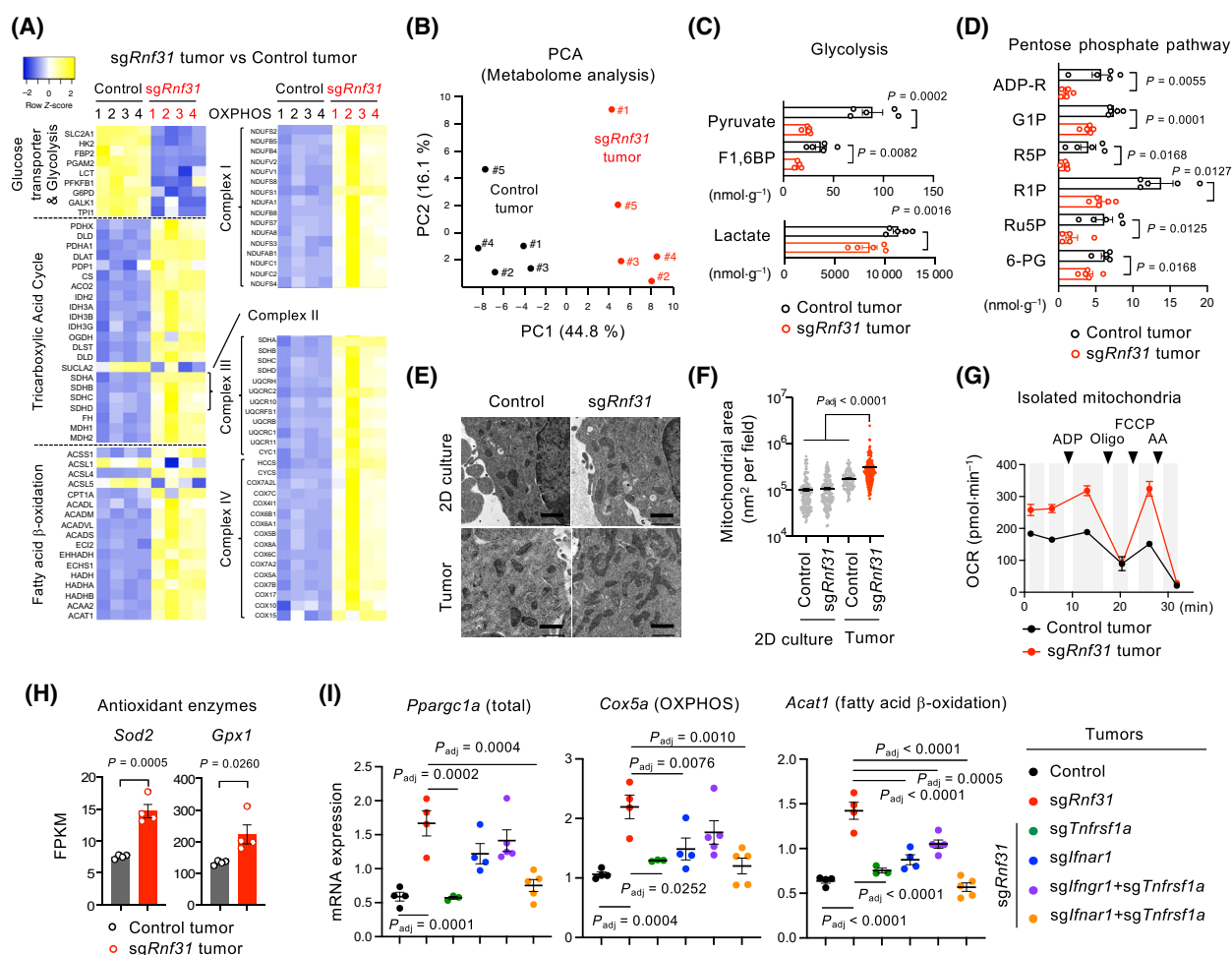
京都大学
KYOTO UNIVERSITY

A Self-archived copy in
Kyoto University Research Information Repository
https://repository.kulib.kyoto-u.ac.jp

京都大学学術情報リポジトリ
KURENAI 紅
Kyoto University Research Information Repository

Linear ubiquitination in cancers

K. Sasaki *et al.*

Fig. 5. Linear ubiquitin rewires aerobic tumor metabolism. (A) Heatmap of transcripts encoding energy-producing metabolic enzymes. (B) Principal component analysis (PCA) of metabolome profiles (n = 5 independent tumors per group). (C, D) Quantitative measurements of the indicated metabolites associated with glycolysis (C) and the pentose phosphate pathway (D). (E) Representative images of TEM analysis. Cultured cells were embedded in Matrigel droplets and then fixed. Data are representative of at least two independent experiments. Scale bar, 2 μm. (F) Measurements of cross-sectional mitochondrial area in the indicated two- or three-dimensional tumor samples. (G) OCR of mitochondria isolated from tumor tissues. (n = 5 independent tumors per group). Oligo, oligomycin A; AA, antimycin A. (H) Expression levels of antioxidant enzymes. (I) Relative expression of the enzymes involved in oxidative metabolism (*Cox5a* and *Acat1*) and mitochondrial biogenesis (*Ppargc1a*, which including all isoforms) in the indicated tumor tissues; control, n = 4; sg*Rnf31*, n = 4; sg*Rnf31* + sg*Tnfrsf1a*, n = 3; sg*Rnf31* + sg*Ifnar1*, n = 4; sg*Rnf31* + sg*Ifngr1* + sg*Tnfrsf1a*, n = 5; sg*Rnf31* + sg*Ifnar1* + sg*Tnfrsf1a*, n = 5. Data are presented as the mean ± SEM. For the statistical analysis of data in C, D, H, the two-tailed unpaired Student's *t*-test was used. One-way ANOVA, followed by Dunnett's multiple comparisons test, was used for the statistical analysis of data in F, I.

TNF and IFNs. The secretion of these cytokines by tumor-associated stromal and immune cells in the majority of solid tumors establishes "tumor-elicited inflammation," one of the hallmarks of cancer [13]. Consequently, linear ubiquitination could be a crucial regulator of tumor cell homeostasis by allowing adaptation to the persistent state of inflammation.

We demonstrated that, in poorly immunogenic melanoma models, linear ubiquitination promotes tumor immune escape via a number of mechanisms. In addition to protecting tumors from immune attack, the linear ubiquitin promotes tissue remodeling and the expansion of tumor necrotic areas. The nature of the tumor necrotic core remains elusive. Recently, the release of the chromatin component HMGB1 by necrotic cells, as a damage-associated molecular pattern (DAMP) molecule, has been shown to promote inflammation and tumor progression [42–44]. Moreover, various studies have reported that intratumoral necrosis positively correlates with poor patient

prognosis in several cancers, including melanoma [45–48]. Furthermore, our findings in melanoma cells also suggest that the necrosis-retaining tumor structure prevents immune attack by limiting IFN responsiveness and up-regulating glycolysis. The fact that a metabolic shift was observed in the sg*Rnf31* tumors may not be too surprising, since tumor cells continuously rewire their metabolism during cancer progression [49–51]. Although the detailed relationship between tumor metabolic plasticity and immune regulation remains enigmatic, recent studies have elegantly demonstrated that the upregulation of glycolysis shapes immune resistance to adoptive T-cell therapy and anti-PD-1 checkpoint blockade therapy in melanoma patients [37,38]. In the present study, the disappearance of the necrotic core, observed in sg*Rnf31* tumors, removed IPRES signatures such as ECM remodeling, cell adhesion, hypoxia, and wound healing. These same IPRES signatures are associated with the non-responder status of patients with metastatic melanoma receiving anti-PD-1 therapy [35]. Thus, it is likely that linear ubiquitination in tumors decreases their immune responsiveness via a variety of mechanisms.

In conclusion, the targeting of linear ubiquitination represents a plausible therapeutic approach to treating solid tumors. Of note, tumor cell death could be potentially accelerated by the tumor itself via autocrine and paracrine proinflammatory cytokine secretion and by the co-administration of therapeutic cytokines or drugs inducing cytokine production. The triggers of linear ubiquitination and the role of various intracellular LUBAC substrates in tumors remain to be investigated. However, this comprehensive study of linear ubiquitination in cancer pathogenesis has provided answers to the long-standing questions of how developing tumors maintain a proinflammatory but immunosuppressive TME and how tumor cells acquire heterogeneity for oncogene-independent immune resistance.

Acknowledgments

Conflict of interest

RM is an employee of Astellas Pharma Inc. The other authors declare that they have no competing interests.

Author contributions

KS and KI designed the experiments, interpreted the results, and wrote the manuscript. KS, YH, and RM performed the experiments. MT assisted with the preparation and sourcing of human cancer FFPE tissue sections used in this study.

Peer Review

The peer review history for this article is available at https://www.webofscience.com/api/gateway/wos/peer-review/10.1002/1873-3468.14623.

Data availability statement

The gene expression omnibus (GEO) accession number for the RNA-seq data reported in this study is GSE206472. The authors declare that all other data originating from this study are available either within the paper or can be obtained upon reasonable request from the corresponding author.

References

1 Yau R and Rape M (2016) The increasing complexity of the ubiquitin code. *Nat Cell Biol* **18**, 579–586.

2 Ye Y, Blaser G, Horrocks MH, Ruedas-Rama MJ, Ibrahim S, Zhukov AA, Orte A, Klenerman D, Jackson SE and Komander D (2012) Ubiquitin chain conformation regulates recognition and activity of interacting proteins. *Nature* **492**, 266–270.

3 Kirisako T, Kamei K, Murata S, Kato M, Fukumoto H, Kanie M, Sano S, Tokunaga F, Tanaka K and Iwai K (2006) A ubiquitin ligase complex assembles linear polyubiquitin chains. *EMBO J* **25**, 4877–4887.

4 Tokunaga F, Sakata SI, Saeki Y, Satomi Y, Kirisako T, Kamei K, Nakagawa T, Kato M, Murata S, Yamaoka S *et al.* (2009) Involvement of linear polyubiquitylation of NEMO in NF-κB activation. *Nat Cell Biol* **11**, 123–132.

5 Haas TL, Emmerich CH, Gerlach B, Schmukle AC, Cordier SM, Rieser E, Feltham R, Vince J, Warnken U, Wenger T *et al.* (2009) Recruitment of the linear ubiquitin chain assembly complex stabilizes the TNF-R1 signaling complex and is required for TNF-mediated gene induction. *Mol Cell* **36**, 831–844.

6 Zinngrebe J, Rieser E, Taraborrelli L, Peltzer N, Hartwig T, Ren H, Kovács I, Endres C, Draber P, Darding M *et al.* (2016) LUBAC deficiency perturbs TLR3 signaling to cause immunodeficiency and autoinflammation. *J Exp Med* **213**, 2671–2689.

7 Boisson B, Laplantine E, Dobbs K, Cobat A, Tarantino N, Hazen M, Lidov HGW, Hopkins G, Du L, Belkadi A *et al.* (2015) Human HOIP and LUBAC deficiency underlies autoinflammation, immunodeficiency, amylopectinosis, and lymphangiectasia. *J Exp Med* **212**, 939–951.

8 Boisson B, Laplantine E, Prando C, Giliani S, Israelsson E, Xu Z, Abhyankar A, Israël L, Trevejo-Nunez G, Bogunovic D *et al.* (2012) Immunodeficiency, autoinflammation and amylopectinosis in humans with inherited HOIL-1 and LUBAC deficiency. *Nat Immunol* **13**, 1178–1186.

9 Gerlach B, Cordier SM, Schmukle AC, Emmerich CH, Rieser E, Haas TL, Webb AI, Rickard JA, Anderton H, Wong WWL *et al.* (2011) Linear ubiquitination prevents inflammation and regulates immune signalling. *Nature* **471**, 591–596.

10 Ikeda F, Deribe YL, Skånland SS, Stieglitz B, Grabbe C, Franz-Wachtel M, van Wijk SJL, Goswami P, Nagy V, Terzic J *et al.* (2011) SHARPIN forms a linear ubiquitin ligase complex regulating NF-κB activity and apoptosis. *Nature* **471**, 637–641.

11 Tokunaga F, Nakagawa T, Nakahara M, Saeki Y, Taniguchi M, Sakata SI, Tanaka K, Nakano H and Iwai K (2011) SHARPIN is a component of the NF-κB-activating linear ubiquitin chain assembly complex. *Nature* **471**, 633–636.

12 Hanahan D and Weinberg RA (2011) Hallmarks of cancer: the next generation. *Cell* **144**, 646–674.

13 Grivennikov SI, Greten FR and Karin M (2010) Immunity, inflammation, and cancer. *Cell* **140**, 883–899.

14 Asai T, Ueda T, Itoh K, Yoshioka K, Aoki Y, Mori S and Yoshikawa H (1998) Establishment and characterization of a murine osteosarcoma cell line (LM8) with high metastatic potential to the lung. *Int J Cancer* **76**, 418–422.

15 Judd NP, Allen CT, Winkler AE and Uppaluri R (2012) Comparative analysis of tumor-infiltrating lymphocytes in a syngeneic mouse model of oral cancer. *Otolaryngol Head Neck Surg* **147**, 493–500.

16 Judd NP, Winkler AE, Murillo-Sauca O, Brotman JJ, Law JH, Lewis JS Jr, Dunn GP, Bui JD, Sunwoo JB and Uppaluri R (2012) ERK1/2 regulation of CD44 modulates oral cancer aggressiveness. *Cancer Res* **72**, 365–374.

17 Sasaki K, Himeno A, Nakagawa T, Sasaki Y, Kiyonari H and Iwai K (2019) Modulation of autoimmune pathogenesis by T cell-triggered inflammatory cell death. *Nat Commun* **10**, 3878.

18 Chang K, Marran K, Valentine A and Hannon GJ (2013) Creating an miR30-based shRNA vector. *Cold Spring Harb Protoc* **2013**, 631–635.

19 Matsumoto ML, Dong KC, Yu C, Phu L, Gao X, Hannoush RN, Hymowitz SG, Kirkpatrick DS, Dixit VM and Kelley RF (2012) Engineering and structural characterization of a linear polyubiquitin-specific antibody. *J Mol Biol* **418**, 134–144.

20 Newton K, Matsumoto ML, Wertz IE, Kirkpatrick DS, Lill JR, Tan J, Dugger D, Gordon N, Sidhu SS, Fellouse FA *et al.* (2008) Ubiquitin chain editing revealed by polyubiquitin linkage-specific antibodies. *Cell* **134**, 668–678.

21 Katsuya K, Oikawa D, Iio K, Obika S, Hori Y, Urashima T, Ayukawa K and Tokunaga F (2019) Small-molecule inhibitors of linear ubiquitin chain assembly complex (LUBAC), HOIPINs, suppress NF-κB signaling. *Biochem Biophys Res Commun* **509**, 700–706.

22 Ohashi Y, Hirayama A, Ishikawa T, Nakamura S, Shimizu K, Ueno Y, Tomita M and Soga T (2008) Depiction of metabolome changes in histidine-starved *Escherichia coli* by CE-TOFMS. *Mol Biosyst* **4**, 135–147.

23 Ooga T, Sato H, Nagashima A, Sasaki K, Tomita M, Soga T and Ohashi Y (2011) Metabolomic anatomy of an animal model revealing homeostatic imbalances in dyslipidaemia. *Mol Biosyst* **7**, 1217–1223.

24 Sugimoto M, Wong DT, Hirayama A, Soga T and Tomita M (2010) Capillary electrophoresis mass spectrometry-based saliva metabolomics identified oral, breast and pancreatic cancer-specific profiles. *Metabolomics* **6**, 78–95.

25 Atkinson DE (1968) The energy charge of the adenylate pool as a regulatory parameter. Interaction with feedback modifiers. *Biochemistry* **7**, 4030–4034.

26 Derr RF and Zieve L (1972) Adenylate energy charge: relation to guanylate energy charge and the adenylate kinase equilibrium constant. *Biochem Biophys Res Commun* **49**, 1385–1390.

27 Tarantino N, Tinevez JY, Crowell EF, Boisson B, Henriques R, Mhlanga M, Agou F, Israël A and Laplantine E (2014) TNF and IL-1 exhibit distinct ubiquitin requirements for inducing NEMO-IKK supramolecular structures. *J Cell Biol* **204**, 231–245.

28 Mantovani A, Biswas SK, Galdiero MR, Sica A and Locati M (2013) Macrophage plasticity and polarization in tissue repair and remodelling. *J Pathol* **229**, 176–185.

29 Eisenbeis CF, Singh H and Storb U (1995) Pip, a novel IRF family member, is a lymphoid-specific, PU.1-dependent transcriptional activator. *Genes Dev* **9**, 1377–1387.

30 Yoshida K, Yamamoto K, Kohno T, Hironaka N, Yasui K, Kojima C, Mukae H, Kadota JI, Suzuki S, Honma K *et al.* (2005) Active repression of IFN regulatory factor-1-mediated transactivation by IFN regulatory factor-4. *Int Immunol* **17**, 1463–1471.

31 Yamagata T, Nishida J, Tanaka T, Sakai R, Mitani K, Yoshida M, Taniguchi T, Yazaki Y and Hirai H (1996) A novel interferon regulatory factor family transcription factor, ICSAT/Pip/LSIRF, that negatively regulates the activity of interferon-regulated genes. *Mol Cell Biol* **16**, 1283–1294.

32 Mattei F, Schiavoni G, Sestili P, Spadaro F, Fragale A, Sistigu A, Lucarini V, Spada M, Sanchez M, Scala S *et al.* (2012) IRF-8 controls melanoma progression by regulating the cross talk between cancer and immune cells within the tumor microenvironment. *Neoplasia* **14**, 1223–1235.

33 Almagro J, Messal HA, Elosegui-Artola A, van Rheenen J and Behrens A (2022) Tissue architecture in tumor initiation and progression. *Trends Cancer* **8**, 494–505.

34 Fiore VF, Krajnc M, Quiroz FG, Levorse J, Pasolli HA, Shvartsman SY and Fuchs E (2020) Mechanics of a multilayer epithelium instruct tumour architecture and function. *Nature* **585**, 433–439.

35 Hugo W, Zaretsky JM, Sun L, Song C, Moreno BH, Hu-Lieskovan S, Berent-Maoz B, Pang J, Chmielowski B, Cherry G *et al.* (2016) Genomic and transcriptomic features of response to anti-PD-1 therapy in metastatic melanoma. *Cell* **165**, 35–44.

36 Henke E, Nandigama R and Ergun S (2019) Extracellular matrix in the tumor microenvironment and its impact on cancer therapy. *Front Mol Biosci* **6**, 160.

37 Harel M, Ortenberg R, Varanasi SK, Mangalhara KC, Mardamshina M, Markovits E, Baruch EN, Tripple V, Arama-Chayoth M, Greenberg E *et al.* (2019) Proteomics of melanoma response to immunotherapy

38 Cascone T, McKenzie JA, Mbofung RM, Punt S, Wang Z, Xu C, Williams LJ, Wang Z, Bristow CA, Carugo A *et al.* (2018) Increased tumor glycolysis characterizes immune resistance to adoptive T cell therapy. *Cell Metab* **27**, 977–987 e974.

39 Ratnikov BI, Scott DA, Osterman AL, Smith JW and Ronai ZA (2017) Metabolic rewiring in melanoma. *Oncogene* **36**, 147–157.

40 Shoag J, Haq R, Zhang M, Liu L, Rowe GC, Jiang A, Koulisis N, Farrel C, Amos CI, Wei Q *et al.* (2013) PGC-1 coactivators regulate MITF and the tanning response. *Mol Cell* **49**, 145–157.

41 Vazquez F, Lim JH, Chim H, Bhalla K, Girnun G, Pierce K, Clish CB, Granter SR, Widlund HR, Spiegelman BM *et al.* (2013) PGC1α expression defines a subset of human melanoma tumors with increased mitochondrial capacity and resistance to oxidative stress. *Cancer Cell* **23**, 287–301.

42 Lee SY, Ju MK, Jeon HM, Jeong EK, Lee YJ, Kim CH, Park HG, Han SI and Kang HS (2018) Regulation of tumor progression by programmed necrosis. *Oxid Med Cell Longev* **2018**, 3537471.

43 Scaffidi P, Misteli T and Bianchi ME (2002) Release of chromatin protein HMGB1 by necrotic cells triggers inflammation. *Nature* **418**, 191–195.

44 Karsch-Bluman A, Feiglin A, Arbib E, Stern T, Shoval H, Schwob O, Berger M and Benny O (2019) Tissue necrosis and its role in cancer progression. *Oncogene* **38**, 1920–1935.

45 Tomes L, Emberley E, Niu Y, Troup S, Pastorek J, Strange K, Harris A and Watson PH (2003) Necrosis and hypoxia in invasive breast carcinoma. *Breast Cancer Res Treat* **81**, 61–69.

46 Richards CH, Mohammed Z, Qayyum T, Horgan PG and McMillan DC (2011) The prognostic value of histological tumor necrosis in solid organ malignant disease: a systematic review. *Future Oncol* **7**, 1223–1235.

47 Jiao D, Cai Z, Choksi S, Ma D, Choe M, Kwon HJ, Baik JY, Rowan BG, Liu C and Liu ZG (2018) Necroptosis of tumor cells leads to tumor necrosis and promotes tumor metastasis. *Cell Res* **28**, 868–870.

48 Bachmann IM, Ladstein RG, Straume O, Naumov GN and Akslen LA (2008) Tumor necrosis is associated with increased αvβ3 integrin expression and poor prognosis in nodular cutaneous melanomas. *BMC Cancer* **8**, 362.

49 Fendt SM, Frezza C and Erez A (2020) Targeting metabolic plasticity and flexibility dynamics for cancer therapy. *Cancer Discov* **10**, 1797–1807.

50 Al-Masri M, Paliotti K, Tran R, Halaoui R, Lelarge V, Chatterjee S, Wang LT, Moraes C and McCaffrey L (2021) Architectural control of metabolic plasticity in epithelial cancer cells. *Commun Biol* **4**, 371.

reveals mitochondrial dependence. *Cell* **179**, 236–250 e218.

51 Lehuede C, Dupuy F, Rabinovitch R, Jones RG and Siegel PM (2016) Metabolic plasticity as a determinant of tumor growth and metastasis. *Cancer Res* **76**, 5201–5208.

Supporting information

Additional supporting information may be found online in the Supporting Information section at the end of the article.

Fig. S1. Validation of linear ubiquitin-specific 1E3.v2 antibody.

Fig. S2. Histological analysis of linear ubiquitin in formalin-fixed, paraffin-embedded human tumor samples.

Fig. S3. Effects of inhibition of linear-ubiquitin-mediated signaling on tumor development.

Fig. S4. Enhanced cytokine vulnerability of LUBAC-deficient tumor cells.

Fig. S5. The sg*Rnf31* tumor is vulnerable to autocrine IFN-γ.

Fig. S6. Phagocytic M2 macrophages eliminate dying sg*Rnf31* tumor cells.

Fig. S7. Decreased cancer-prone characteristics of sg*Rnf31* tumors.

Fig. S8. sg*Rnf31* tumors down-regulate their hypoxia response and ECM remodeling.

Fig. S9. Activation of mitochondrial metabolism in sg*Rnf31* tumors.

Fig. S10. Blockade of linear-ubiquitin-mediated inflammatory tolerance remodels necrotic tumor architecture and alters its immunogenicity.